Euclid preparation. XXXII. Evaluating the weak lensing cluster mass biases using the Three Hundred Project hydrodynamical simulations

Euclid Collaboration; Euclid Collaboration, The Pierre Auger; Giocoli, C.; Meneghetti, M.; Rasia, E.; Borgani, S.; Despali, G.; Lesci, G. F.; Marulli, F.; Moscardini, L.

Astronomy & Astrophysics manuscript no. paper
October 19, 2023

Euclid preparation. XXXII. Evaluating the weak lensing cluster mass biases using the Three Hundred Project hydrodynamical simulations

Euclid Collaboration: C. Giocoli[1,2⋆], M. Meneghetti[1,2], E. Rasia[3,4], S. Borgani[3,5,6,4], G. Despali[7], G. F. Lesci[8,1], F. Marulli[8,1,2], L. Moscardini[8,1,2], M. Sereno[1,2], W. Cui[9,10,11], A. Knebe[9,10,12], G. Yepes[9,10], T. Castro[3,6,4], P.-S. Corasaniti[13], S. Pires[14], G. Castignani[8,1], T. Schrabback[15,16], G. W. Pratt[17], A. M. C. Le Brun[13], N. Aghanim[18], L. Amendola[19], N. Auricchio[1], M. Baldi[8,1,2], C. Bodendorf[20], D. Bonino[21], E. Branchini[22,23], M. Brescia[24], J. Brinchmann[25], S. Camera[26,27,21], V. Capobianco[21], C. Carbone[28], J. Carretero[29,30], F. J. Castander[31,32], M. Castellano[33], S. Cavuoti[34,35], R. Cledassou[36,37], G. Congedo[11], C.J. Conselice[38], L. Conversi[39,40], Y. Copin[41], L. Corcione[21], F. Courbin[42], M. Cropper[43], A. Da Silva[44,45], H. Degaudenzi[46], J. Dinis[45,44], F. Dubath[46], X. Dupac[39], S. Dusini[47], S. Farrens[48], S. Ferriol[41], P. Fosalba[32,31], M. Frailis[3], E. Franceschi[1], M. Fumana[28], S. Galeotta[3], B. Garilli[28], B. Gillis[11], A. Grazian[49], F. Grupp[20,50], S. V. H. Haugan[51], W. Holmes[52], A. Hornstrup[53,54], K. Jahnke[55], M. Kümmel[50], S. Kermiche[56], M. Kilbinger[48], M. Kunz[57], H. Kurki-Suonio[58,59], S. Ligori[21], P. B. Lilje[51], I. Lloro[60], E. Maiorano[1], O. Mansutti[3], O. Marggraf[16], K. Markovic[52], R. Massey[61], S. Maurogordato[62], S. Mei[63], E. Merlin[33], G. Meylan[42], M. Moresco[8,1], E. Munari[3], S.-M. Niemi[64], J. Nightingale[61], T. Nutma[65,66], C. Padilla[29], S. Paltani[46], F. Pasian[3], K. Pedersen[67], V. Pettorino[48], G. Polenta[68], M. Poncet[36], L. A. Popa[69], F. Raison[20], A. Renzi[70,47], J. Rhodes[52], G. Riccio[34], E. Romelli[3], M. Roncarelli[1], E. Rossetti[71], R. Saglia[50,20], D. Sapone[72], B. Sartoris[50,3], P. Schneider[16], A. Secroun[56], S. Serrano[32,73], C. Sirignano[70,47], G. Sirri[2], L. Stanco[47], J.-L. Starck[14], P. Tallada-Crespí[74,30], A.N. Taylor[11], I. Tereno[44,75], R. Toledo-Moreo[76], F. Torradeflot[74,30], I. Tutusaus[77], E. A. Valentijn[66], L. Valenziano[1,2], T. Vassallo[3], Y. Wang[78], J. Weller[50,20], G. Zamorani[1], J. Zoubian[56], S. Andreon[79], S. Bardelli[1], A. Boucaud[63], E. Bozzo[46], C. Colodro-Conde[80], D. Di Ferdinando[2], G. Fabbian[81,82], M. Farina[83], H. Israel[84], E. Keihänen[85], V. Lindholm[58,59], N. Mauri[86,2], C. Neissner[29], M. Schirmer[55], V. Scottez[87,88], M. Tenti[89], E. Zucca[1], Y. Akrami[90,91,92,93,94], C. Baccigalupi[95,4,3,6], M. Ballardini[96,97,1], F. Bernardeau[98,99], A. Biviano[3,4], A. S. Borlaff[100], C. Burigana[96,101,89], R. Cabanac[77], A. Cappi[1,62], C. S. Carvalho[75], S. Casas[102], K. C. Chambers[103], A. R. Cooray[104], H.M. Courtois[105], S. Davini[106], S. de la Torre[107], G. De Lucia[3], G. Desprez[46,108], H. Dole[18], J. A. Escartin[20], S. Escoffier[56], I. Ferrero[51], F. Finelli[1,89], L. Gabarra[70,47], K. Ganga[63], J. Garcia-Bellido[90], K. George[109], F. Giacomini[2], G. Gozaliasl[58], H. Hildebrandt[110], I. Hook[111], A. Jimenez Muñoz[112], B. Joachimi[113], J. J. E. Kajava[114], V. Kansal[14], C. C. Kirkpatrick[85], L. Legrand[57], A. Loureiro[11,94], J. Macias-Perez[112], M. Magliocchetti[83], G. Mainetti[115], R. Maoli[116,33], S. Marcin[117], M. Martinelli[33,118], N. Martinet[107], C. J. A. P. Martins[119,25], S. Matthew[11], L. Maurin[18], R. B. Metcalf[8,1], P. Monaco[5,3,6,4], G. Morgante[1], S. Nadathur[120], A.A. Nucita[121,122,123], L. Patrizii[2], A. Peel[42], J. Pollack[124,63], V. Popa[69], C. Porciani[16], D. Potter[125], M. Pöntinen[58], P. Reimberg[87], A.G. Sánchez[20], Z. Sakr[77,19,126], A. Schneider[125], E. Sefusatti[3,6,4], A. Shulevski[65,66], A. Spurio Mancini[43], J. Stadel[125], J. Steinwagner[20], J. Valiviita[58,59], A. Veropalumbo[127], M. Viel[95,4,3,6], I. A. Zinchenko[50]

(Affiliations can be found after the references)

October 19, 2023

ABSTRACT

The photometric catalogue of galaxy clusters extracted from ESA *Euclid* data is expected to be very competitive for cosmological studies. Using state-of-the-art hydrodynamical simulations, we present systematic analyses simulating the expected weak lensing profiles from clusters in a variety of dynamic states and at wide range of redshifts. In order to derive cluster masses, we use a model consistent with the implementation within the Euclid Consortium of the dedicated processing function and find that, when jointly modelling mass and the concentration parameter of the Navarro–Frenk–White halo profile, the weak lensing masses tend to be, on average, biased low by 5–10% with respect to the true mass, up to $z = 0.5$. Using a fixed value for the concentration $c_{200} = 3$, the mass bias is diminished below 5%, up to $z = 0.7$, along with its relative uncertainty. Simulating the weak lensing signal by projecting along the directions of the axes of the moment of inertia tensor ellipsoid, we find that orientation matters: when clusters are oriented along the major axis, the lensing signal is boosted, and the recovered weak lensing mass is correspondingly overestimated. Typically, the weak lensing mass bias of individual clusters is modulated by the weak lensing signal-to-noise ratio, related to the redshift evolution of the number of galaxies used for weak lensing measurements: the negative mass bias tends to be larger toward higher redshifts. However, when we use a fixed value of the concentration parameter, the redshift evolution trend is reduced. These results provide a solid basis for the weak-lensing mass calibration required by the cosmological application of future cluster surveys from *Euclid* and *Rubin*.

Key words. Galaxy Clusters, Gravitational Lensing, Photometric Galaxies

1. Introduction

The abundance and the spatial distribution of galaxy clusters as a function of redshift represent important cosmological probes for future wide-field surveys, and particularly for the ESA *Euclid* mission (Laureijs et al. 2011; Euclid Collaboration: Scaramella et al. 2022). Cluster cosmological studies (e.g., Allen et al. 2011) will complement the two main probes based on weak lensing cosmic shear and galaxy clustering, improving the figure of merit of the derived cosmological parameters (see e.g., Sartoris et al. 2016).

Galaxy clusters form close to the mass density peaks of the initial matter density fluctuations and accrete mass through cosmic time as a consequence of repeated merging events (Tormen 1998; Tormen et al. 2004; Giocoli et al. 2012b; Kravtsov & Borgani 2012). In the present day, clusters represent the largest virialised structures in the Universe. Their structural properties (Giocoli et al. 2008; Despali et al. 2014, 2017) are important tracers of their assembly history and dynamical state. For example, a lower value of their concentration parameter and a higher mass fraction in substructures are typical of late-forming systems. On the contrary, fewer substructures and high concentrations are ordinary for clusters that assemble most of their mass at higher redshifts, which appear more regular and are rounder (Gao et al. 2004; De Lucia et al. 2004; Giocoli et al. 2010a; Bonamigo et al. 2015; Mostoghiu et al. 2019).

The ESA *Euclid* mission, complemented by the multiband photometric support from the ground by various observational facilities will be able to identify galaxy clusters using two complementary algorithms: `AMICO` and `PZWav` (Euclid Collaboration: Adam et al. 2019). While the `AMICO` (Adaptive Matched Identifier of Clustered Objects) algorithm (Bellagamba et al. 2011, 2018; Maturi et al. 2019) uses an enhanced matched filter method that looks for cluster candidates by convolving the 3D galaxy distribution with a redshift-dependent filter, `PZWav` (Gonzalez 2014) is a wavelet transform-based code that searches for overdensities on fixed physical scales. The two methods have been extensively studied thanks to dedicated activities and performance challenges (Euclid Collaboration: Adam et al. 2019) that guarantee both methods have a purity and completeness of at least 80 per cent for systems with a mass larger than $M_{200} = 10^{14}\,M_{\odot}$[1] and redshift $z < 2$. Being complementary, the matching procedures of the two detection algorithms are expected to generate a highly pure and complete catalogue.

The use of clusters as a cosmological tool relies on the accuracy with which we can recover their true mass (Pratt et al. 2019, for a review). The mass enclosed within a given overdensity can be measured in numerical simulations (Sheth & Tormen 1999; Springel et al. 2001; Tormen et al. 2004), and it is used to build up analytical functions to describe the number density of haloes as a function of mass and redshift (Tinker et al. 2008; Despali et al. 2016; Klypin et al. 2016; Chua et al. 2017; Bocquet et al. 2020; Ondaro-Mallea et al. 2022; Euclid Collaboration: Castro et al. 2022). However, from an observational perspective, we have to rely on mass proxy estimates that could be scattered and biased. Typically, these biases and scatters are due to the simple analytical models used to characterise the complexity of the astrophysical processes taking place in the cluster environments (Becker & Kravtsov 2011; Grandis et al. 2021). In addition, the scatter in the cluster richness [2]-mass relation could increase because of different feedback and quenching mechanisms taking place in the highly-dense cluster environments.

The dynamics of cluster galaxies has been extensively used in multiple dedicated observations to characterise the cluster mass (Biviano et al. 2006, 2013; Bocquet et al. 2015; Capasso et al. 2019). This method may suffer from the presence of interlopers that may systematically bias the derived dynamical mass. This limitation could be alleviated by removing clusters with significant evidence of sub-structures and groups along the line of sight or by selecting early-type galaxies as spectroscopic targets (Damsted et al. 2023).

The hydrostatic masses derived from X-ray observations and assuming a model-based hydrostatic equilibrium are biased low with respect to the true mass by around 20-25 per cent, as discussed in different studies based on hydrodynamical simulations (Lau et al. 2009; Meneghetti et al. 2010b; Rasia et al. 2012; Biffi et al. 2016; Ansarifard et al. 2020; Barnes et al. 2021; Gianfagna et al. 2021). The inclusion of turbulent and non-thermal pressure support in the model attenuates the discrepancies (Angelinelli et al. 2020; Ettori & Eckert 2022), but at the price of dedicated high-resolution multiwavelength follow-up observations of the cluster environment.

Gravitational lensing, particularly in the weak regime, is the primary method to be used within the Euclid Collaboration to weigh clusters. Since lensing does not rely on any assumption on the dynamical state of the various mass components of the cluster, it provides, in principle, an unbiased estimate of the projected matter density distribution (Bartelmann & Schneider 2001; Bartelmann 2010). However, it suffers from deprojection effects when converting the derived weak lensing mass to the actual three-dimensional one (Meneghetti et al. 2008; Giocoli et al. 2012, 2014). Dedicated works have been recently carried out, based on state-of-the-art hydrodynamical simulations, to assess the reliability of the weak lensing mass from future wide-field surveys (Grandis et al. 2019) and to quantify the effects of baryonic physics (Henson et al. 2017; Grandis et al. 2021; Cromer et al. 2022). On the other hand, Martizzi et al. (2014); Cusworth et al. (2014); Velliscig et al. (2014); Bocquet et al. (2016a); Debackere et al. (2021); Castro et al. (2021) have studied the impact of baryons on the halo mass function and their effect on the cosmological parameter estimates using cluster counts. Typically, weak lensing mass biases are, in principle, not problematic, as long estimated from representative simulated cluster samples (e.g. Applegate et al. 2016; Schrabback et al. 2018; Grandis et al. 2019; Sommer et al. 2022) and self-consistently accounted for in cluster scaling relation and cosmology analyses (e.g. Dietrich et al. 2019; Bocquet et al. 2019; Schrabback et al. 2021; Chiu et al. 2022; Zohren et al. 2022).

Recent works by Debackere et al. (2022a,b) have shown the potential of weak lensing aperture mass to recover the projected mass density distribution of galaxy cluster regions. The method does not rely on any particular mass density profile model but needs to be tuned and trained on large sample cosmological simulations. This approach also requires us to rewrite all likelihoods of the cluster cosmology pipeline in terms of projected quantities instead of 3D masses (see also Giocoli et al. 2012).

Thanks to the high efficiency, the unprecedented combination of spatial resolution and sensitivity of the VIS instrument (Cropper et al. 2016) onboard the *Euclid* satellite, we are expected to reach a number density of sources for weak lensing

⋆ e-mail: carlo.giocoli@inaf.it

[1] The mass within the radius that encloses 200 times the critical density of the universe at a given redshift.

[2] Defined as the total number of member galaxies within the cluster radius R_{200}, above a typical characteristic luminosity.

studies of 30 galaxies per square arcminute. This large number density of sources will give us the possibility to recover weak lensing masses for individual massive clusters. However, going toward high-redshift clusters $z > 0.6$, the dearth of available sources requires stacking their signals, for well-defined richness and redshift bins, to increase the signal-to-noise and the accuracy of the (stacked) mass.

In this paper, we use a large sample of cosmological hydrodynamic simulations of clusters from The Three Hundred Collaboration (Cui et al. 2018), to make a systematic assessment of the weak lensing mass bias of clusters. We study how the modelling function parameters (truncation radius, concentration, etc.) affect the recovered weak lensing mass; in addition, we investigate how the mass bias depends on the true mass of the cluster, on its redshift, and, particularly, on its orientation with respect to the line of sight, which represents the largest source of intrinsic scattering at fixed cluster mass. We would like to underline that the results here presented have been obtained assuming a specific modelling of the feedback inside clusters, and they could be sensitive to this choice. However, Grandis et al. (2021) have estimated that different hydrodynamic solvers may have an impact on the weak lensing mass bias below 5%. We have planned a future work to systematically assess this.

The paper is organised as follows: in Sect. 2 we introduce the cluster simulations summarising the cluster properties that we will use for this work; in Sect. 3 we present our lensing pipeline and how we simulate the expected signal from the ESA *Euclid* data; Sect. 4 discusses the results using our modelling functions. In Sect. 5 we summarise and conclude.

2. The Three Hundred simulation data-set

In this work, we rely on dedicated weak lensing simulations of clusters extracted from the re-simulated regions by the Three Hundred Collaboration (Cui et al. 2018, 2022). The data set consists of 324 regions centred on the most massive clusters ($M_{200} \gtrsim 8 \times 10^{14}\,h^{-1}\,M_\odot$) identified at $z = 0$ in the DM-only MDPL2 MultiDark simulation (Klypin et al. 2016), with a box-size of 1 Gpc on a side. The parent simulation was run adopting the cosmological parameters as derived by the *Planck* mission (Planck Collaboration 2016): $\Omega_\mathrm{m} = 0.307$, $\Omega_\mathrm{b} = 0.048$, $\Omega_\Lambda = 0.693$, $h = 0.678$, $\sigma_8 = 0.823$ and $n_\mathrm{s} = 0.96$. For each selected region, initial conditions with multiple levels of mass refinements were generated using the `GINNUNGAGAP` code[3]. Within the highest resolution Lagrangian region – at least five times larger than the cluster virial radius – particles are divided into dark matter (DM) and gas types according to the considered cosmological baryon fraction: $m_\mathrm{dm} = 12.7 \times 10^8\,h^{-1}\,M_\odot$ and $m_\mathrm{gas} = 2.36 \times 10^8\,h^{-1}\,M_\odot$, respectively.

The resolution outside this region is degraded to reduce the computational cost with respect to the parent original simulation. It is worth mentioning that each re-simulated region, with a typical radius of $15\,h^{-1}$ Mpc from the centre, may contain additional groups and filaments not physically associated and not gravitationally bound to the virialised cluster but important for total projected mass quantity studies.

The evolution of the particle distribution from the initial-conditions ($z = 120$) until the present time was followed using `GADGET-X`, based on the gravity solved `GADGET-3` Tree-PM code. The code uses an improved smooth-particle hydrodynamics (SPH) scheme (Beck et al. 2016) to follow the evolution of the gas component with artificial thermal diffusion, time-dependent artificial viscosity, high-order Wendland C4 interpolating kernel and wake-up scheme. These improvements increase the SPH capability of following gas-dynamical instabilities and mixing processes by better describing the discontinuities and reducing the clumpiness instability of gas.

As described in more detail in Rasia et al. (2015), the simulations include metallicity-dependent radiative cooling and the effect of a uniform time-dependent UV background (Planelles et al. 2014). The sub-resolution star formation model follows Springel & Hernquist (2003), and the metal production from SN-II, SN-Ia, and asymptotic-giant-branch stars use the original recipe by Tornatore et al. (2007). The active galactic nucleus feedbacks and supermassive black hole accretions are modelled with the implementations presented in Steinborn et al. (2015).

At each simulation snapshot, the haloes were identified using `AHF` (Amiga Halo Finder: Knollmann & Knebe 2009) which consistently accounts for DM, star, and gas particles in finding and characterising halo properties. For each halo, the algorithm defines M_{200}, using a spherical overdensity algorithm, i.e., the mass within the radius R_{200} which encloses 200 times the critical comoving density of the universe $\rho_\mathrm{c}(z)$ at the corresponding redshift,

$$M_{200} = \frac{4\pi}{3} R_{200}^3\, 200\, \rho_\mathrm{c}(z)\,. \tag{1}$$

For each halo, we consider subhaloes whose centres lie within the corresponding halo radius R_{200}. The subhalo properties are defined at the truncation radius R_t (the outer edge of the system) and hence mass, density profile, velocity dispersion, rotation curve are calculated using the gravitationally bound particles inside this radius (Tormen et al. 1998). In particular, for each halo in this work we make use of:

- the mass fraction in substructures f_sub accounting for the full subhalo hierarchy of subhaloes within subhaloes;
- the halo virial circular velocity $V_{200} = \sqrt{\dfrac{GM_{200}}{R_{200}}}$;
- the maximum circular velocity V_max;
- the radius R_max at which the maximum circular velocity is attained;
- the centre-of-mass offset x_off – expressed in the unit of the halo radius R_{200}, defined as the difference between the centre-of-mass and the maximum density peak of the halo, which we denote as the cluster centre;
- the virial ratio $\eta \equiv (2T - E_\mathrm{s})/|W|$, where T indicates the total kinetic energy, E_s the energy from surface pressure and W refers to the total potential energy;
- the eigenvalues and the eigenvectors of the moment of inertia tensor.

The Navarro–Frenk–White (hereafter NFW) density profile (Navarro et al. 1996, 1997), depending on the host halo mass and concentration is defined as:

$$\rho_\mathrm{NFW}(r|M_{200}, c_{200}) = \frac{\rho_\mathrm{s}}{(r/r_\mathrm{s})(1 + r/r_\mathrm{s})^2} \tag{2}$$

where ρ_s is defined as:

$$\rho_\mathrm{s} = \frac{M_{200}}{4\pi r_\mathrm{s}^3} \frac{1}{\ln(1 + c_{200}) - c_{200}/(1 + c_{200})}\,, \tag{3}$$

and $r_\mathrm{s} = R_{200}/c_{200}$.

From the global halo quantities, we adopt two prescriptions to define the halo concentration. Assuming that the halo density

[3] https://github.com/ginnungagapgroup/ginnungagap

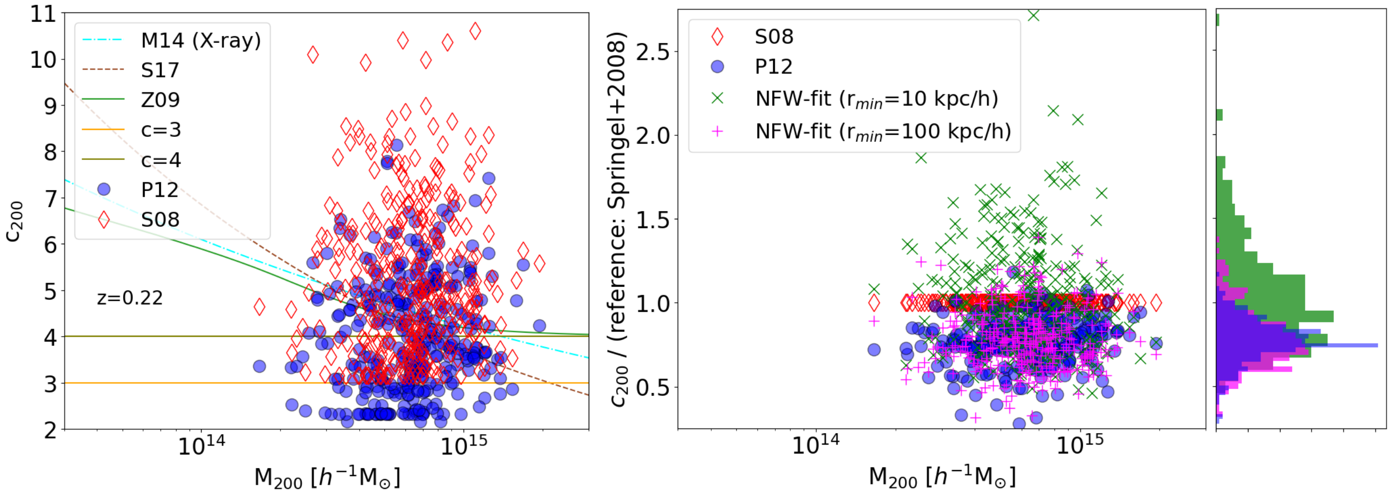

Fig. 1. *Left panel*: concentration-mass relation of the clusters at $z = 0.22$. The blue and red data points represent the concentration values computed using the Prada et al. (2012, hereafter P12) and Springel et al. (2008b, hereafter S08) relations, respectively. The various lines display different concentration-mass relation models computed at $z = 0.22$. *Right panel*: ratio between the measured concentration, using different methods compared with respect to the Springel et al. (2008b) formalism. Green crosses and magenta pluses display the case in which we compute the concentration by fitting the differential logarithmic density profile outside 10, and 100 h^{-1} kpc, respectively.

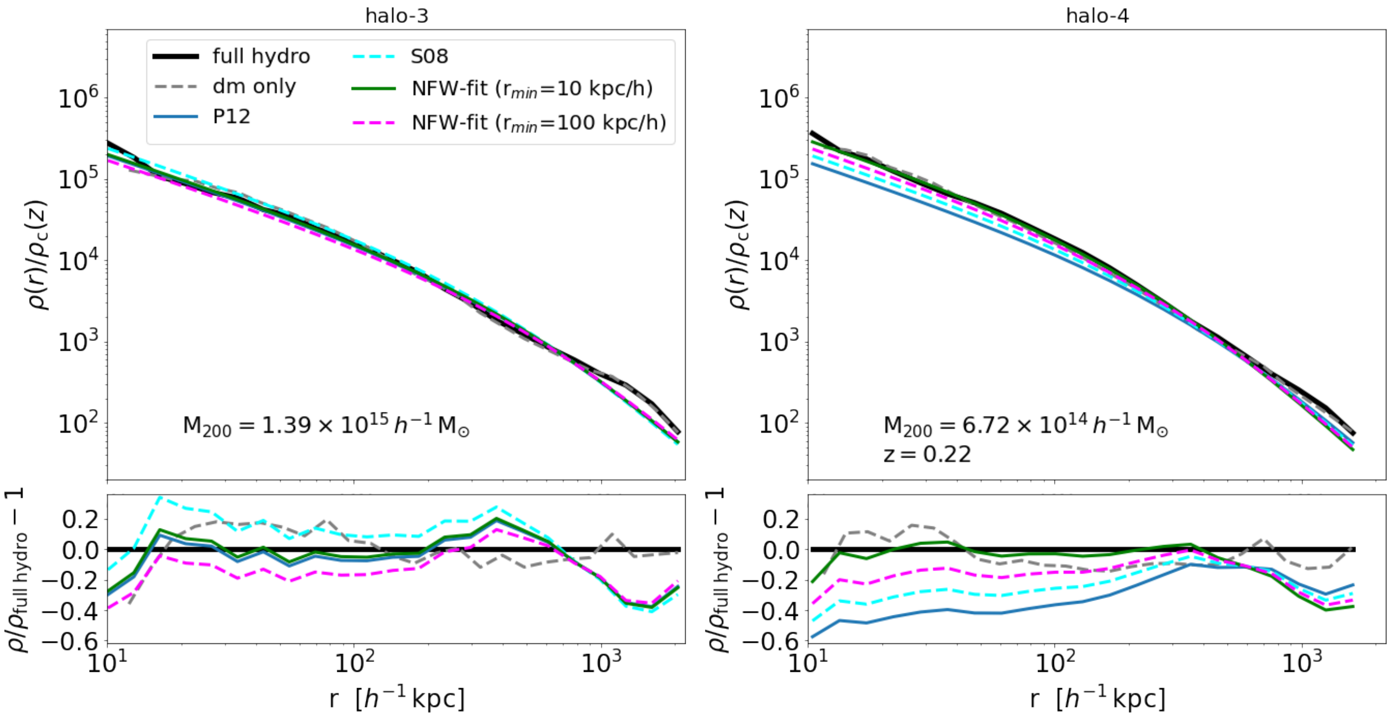

Fig. 2. Spherical averaged density profiles of halo-3 and halo-4. In each panel, the solid black curve displays the total matter density profile of the full hydrodynamical runs, as considered in this work. For comparison, the dashed grey curve shows the profile of the dark matter only runs. With solid blue and dashed cyan lines, we exhibit the NFW profiles assuming concentrations as computed using P12 and S08 formalisms, respectively. With solid green and dashed magenta lines, we show the NFW profiles where concentrations have been computed fitting the logarithm profile outside 10 and 100 h^{-1} *kpc*, respectively. Profiles extend up to the halo virial radius R_{200}, as computed by `AHF`.

profile follows an NFW relation, Springel et al. (2008a, hereafter S08) defines the halo concentration numerically by solving

$$\frac{200}{3} \frac{c_{200}^3}{\ln(1 + c_{200}) - c_{200}/(1 + c_{200})} = 14.426 \left(\frac{V_{\max}}{H(z)\, R_{\max}} \right)^2 , \quad (4)$$

where $H(z)$ represents the Hubble parameter at the corresponding redshift.

Following a simpler version of the density profile parametrisation, Prada et al. (2012, hereafter P12) describe the halo concentration in terms of the velocity ratio only as follows:

$$\frac{V_{\max}}{V_{200}} = \sqrt{\frac{0.216\, c_{200}}{\ln(1 + c_{200}) - c_{200}/(1 + c_{200})}} \,. \quad (5)$$

The two above definitions of concentration coincide if the halo is perfectly defined by a spherical NFW profile.

Different post-processing analyses of numerical simulations have historically adopted different concentration definitions. In

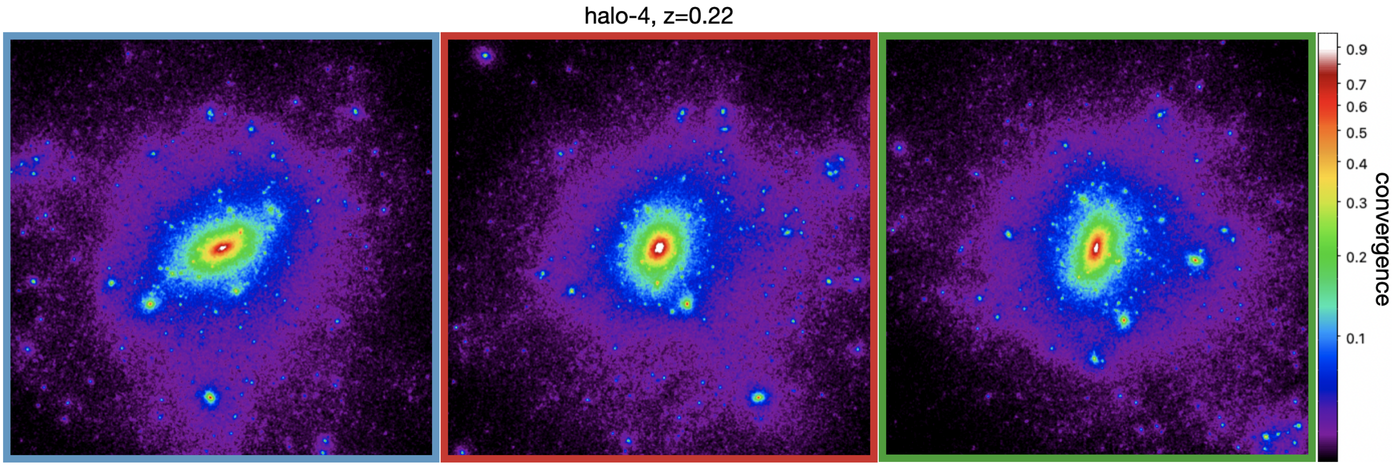

Fig. 3. Convergence maps of the three considered random projections of a cluster, namely the halo-4 at $z = 0.22$. The left, central and right panels show the projections along the z, y, and x axis coordinates of the re-simulated box. The source redshift of the map is fixed at $z_s = 3$. The size of the field of view is 5 Mpc (3.4 h^{-1} Mpc) on a side, 10 Mpc along the line-of-sight. The map resolution is 2048 pixels on a side.

this paragraph, we compare models based on different concentration definitions employed in our study. The left panel of Fig.1 displays the concentration-mass relation for the Three Hundred clusters at $z = 0.22$. The red diamonds and the blue-filled circles refer to the concentration parameters computed using Eq. (4) and (5), respectively. The figure also contains various predictions at the corresponding redshift, obtained after modelling the results from numerical simulations (Zhao et al. 2009; Meneghetti et al. 2014, hereafter Z09, M14, respectively) or interpreting observational data (Sereno et al. 2017, hereafter S17). In particular, for the Z09 model we adopt the Giocoli et al. (2012b) formalism to follow the main halo mass accretion history back in time. From the figure, we notice that the two adopted models for the concentration predict a different value at fixed halo mass: at this redshift on average Prada et al. (2012) underestimates the concentration parameter by approximately 20% with respect to Springel et al. (2008a). This is a manifestation of the fact that the clusters, particularly in hydrodynamical simulations, deviate from the perfect NFW profile for which the two models would have the same concentration. In addition, the S08 model, written in terms of the radius $R_{\rm max}$, tends to be more sensitive to baryonic physics and adiabatic contraction than P12, which is parametrised only in terms of velocities, the average relative difference between the two models varies with redshift. In the right panel of Fig. 1, we display the ratio between various concentration definitions with respect to the prediction by Springel et al. (2008a). Green crosses and magenta plus signs correspond to the concentration computed by fitting the logarithm of the total differential density profile, computed by the `AHF`, outside 10 and 100 h^{-1}kpc from the centre, respectively: binning procedures and reference models may impact the concentration definition (Meneghetti & Rasia 2013). Density profiles are very sensitive to baryonic effects at small radii. Higher concentration parameters result from a steepening of the inner slope of the profile (Schaller et al. 2015b,a; Ahad et al. 2021; Jung et al. 2022) due to the adiabatic contraction, whose effect is mitigated by the AGN feedback but not completely suppressed (Rasia et al. 2013). Since this paper aims at studying the WL mass reconstruction and the projected density profiles are not reliable within the central 100 kpc – noticing that the corresponding concentrations are in good agreement with P12. For the rest of this work, we will also use S08 as a reference to give an idea of the theoretical uncertainties.

In Fig. 2, we show the spherical average density profiles of two clusters: halo-3 (on the left) and halo-4 (on the right). In each panel, the black solid and dashed grey curves refer to the total density profile of the full hydrodynamical simulations and of the corresponding dark matter-only runs. Profiles extend up to R_{200} defined as the radius enclosing 200 times the critical density. Solid blue and dashed cyan curves display the NFW profiles using the concentration values as derived from the P12 and S08 relations, respectively. With solid green and dashed magenta lines, we display the NFW profiles where concentration has been derived modelling the logarithmic density profile outside 10 and 100 h^{-1} kpc, respectively. From the figure, we notice that while for halo-3 the solid blue and green lines describe relatively well the total mass density profile of the cluster, for halo-4 only the green line well represents the matter density distribution. This could be due to the fact that while the halo-3 has an inner slope $\mathrm{d}\log\rho/\mathrm{d}\log r$ close to -1, the cluster halo-4 has a steeper slope toward the centre. We can also notice that the density in the outskirts of the clusters is higher than expected from the NFW profile due to the presence of substructures. Those differences reduce when looking at projected quantities, highlighting that the NFW prescription is sufficient for the analysis in this paper.

We would also like to underline that the extrapolation of those 3D uncertainties into projected quantities is not straightforward and may require some reference concentration-mass relation model to be adopted (Hoekstra et al. 2013; Simet et al. 2017a,b; Kiiveri et al. 2021; Sommer et al. 2022). We will describe how those impact the recovered weak lensing mass bias in the next section.

3. Cluster weak lensing simulations

In order to build up the mass maps, we proceed as follows. From the `AHF` catalogues, we read the positions of the halo centres in comoving units (x_c, y_c, z_c) and then the particle positions with associated masses and types from the corresponding snapshot file. Each snapshot contains dark matter, gas, star, and black hole particles. For each cluster, we consider three random lines of sight corresponding to the axes of the simulation box, along which we project the cluster particles on a perpendicular plane centred on the cluster centre. We consider particles in a slice of depth ±5 Mpc (3.4 h^{-1} Mpc) in front and behind the cluster. The maps have a final size of 5 Mpc on a side, resolved with 2048^2

pixels and are produced using `Py-SPHViewer` (for more details we refer to Benitez-Llambay 2015). The choice of the size of the field of view is motivated by the fact that we are mainly interested in modelling the projected matter density distribution of the main cluster without being much affected by the additional source of uncertainty associated to the large-scale matter density distribution along the line of sight (Hoekstra 2001, 2003). This value also represents a reasonable compromise to avoid influence due to low-resolution particles in the re-simulated box. In addition, it is worth stressing that the scatter in the weak lensing mass bias could be underestimated with respect to what is measured by Becker & Kravtsov (2011), who used a larger line-of-sight integration.

The convergence κ is obtained from the mass map by dividing the mass per pixel by its associated area to obtain the surface density $\Sigma(\boldsymbol{\theta})$ and by the critical surface density $\Sigma_{\rm crit}$ (Bartelmann & Schneider 2001) that can be read as:

$$\Sigma_{\rm crit} \equiv \frac{c^2}{4\pi G}\frac{D_{\rm s}}{D_{\rm l} D_{\rm ls}}\,, \tag{6}$$

where $D_{\rm l}$, $D_{\rm s}$, and $D_{\rm ls}$ are the observer-lens, observer-source, and source-lens angular diameter distances, respectively; c represents the speed of light and G the universal gravitational constant. The critical surface density is a function of the redshift of the lens and of the source. Our reference weak lensing maps have been created assuming a fixed source redshift $z_{\rm s} = 3$.

In Fig. 3, we show three convergence maps of the same cluster, namely halo-4 at $z = 0.22$. The left, central and right panels display the system projected along the z, y, and x-axis of the comoving re-simulated box, respectively. Since there is no particular selection with respect to the triaxial properties of the cluster haloes, these projections can be seen as *random* projections and as such we will name them as proj0, proj1, proj2, respectively, in the following.

For each cluster, redshift, and projection, we generate weak lensing convergence maps, specifically, we consider 9 redshifts from $z = 0.12$ to $z = 0.98$ as listed in Table 1.

Table 1. List of the analysed simulation snapshots (first column) and the corresponding redshifts (second column). The third column specifies the average number of background galaxies used to construct the simulated weak lensing shear profile as expected by the *Euclid*-ESA mission to lay beyond a cluster at a given redshift. The fourth expresses the square root of the average number of background galaxies rescaled by the ratio of angular diameter distances, relevant for quantifying lensing detectability. The last column shows the average cluster mass at the corresponding redshift, in the unit of $10^{14}\,h^{-1}\,M_{\odot}$.

snap.	z	$n_{\rm g}^a$	$\sqrt{n_{\rm g}}\,D_{\rm ls}/D_{\rm s}^b$	$\langle M_{200}\rangle^c$
123	0.12	30	5.04	7.85
119	0.22	29	4.62	6.77
115	0.33	28	4.20	5.77
113	0.39	27	3.95	5.32
110	0.49	26	3.60	4.66
107	0.59	24	3.22	3.99
104	0.70	22	2.65	3.38
101	0.82	19	2.40	2.83
098	0.94	17	2.07	2.38

[a] [$arcmin^{-2}$]
[b] [$arcmin^{-1}$]
[c] [$10^{14}\,h^{-1}\,M_{\odot}$]

From the convergence κ, we define the lensing potential ψ, using the two-dimensional Poisson equation as:

$$\Delta_{\theta}\psi(\boldsymbol{\theta}) = 2\,\kappa(\boldsymbol{\theta})\,, \tag{7}$$

that we numerically solve in Fourier space using the Fast Fourier Transform (FFT) method. Since the FFT algorithm assumes periodic conditions on the boundaries of the map, we zero-pad the exterior of the convergence map by 0.5 Mpc before computing the discrete Fourier transform and then remove the region from the final result.

From the lensing potential ψ, we can then define the two components (γ_1, γ_2) of the pseudo-vector shear, as:

$$\gamma_1(\boldsymbol{\theta}) = \frac{1}{2}\left(\frac{\partial^2\psi(\boldsymbol{\theta})}{\partial x^2} - \frac{\partial^2\psi(\boldsymbol{\theta})}{\partial y^2}\right)\,, \tag{8}$$

$$\gamma_2(\boldsymbol{\theta}) = \frac{\partial^2\psi(\boldsymbol{\theta})}{\partial x\,\partial y}\,, \tag{9}$$

where x and y represent the two components of the vector $\boldsymbol{\theta}$.

For each cluster, we use the shear maps to simulate an observed differential surface mass density profile by randomly sampling the field of view with a given number density of expected background sources.

In our analysis, we adopt a background density of sources for weak lensing following the predicted distribution for the ESA *Euclid* wide-field survey normalised to the total value of 30 galaxies per square arcmin (Laureijs et al. 2011). In the third column of Table 1 we report the average number of background sources beyond each considered cluster redshift, whose corresponding snapshot number is displayed in the first column.

The approach of randomly sampling the shear field has been chosen to mimic the expected average profile of a cluster from a *Euclid* wide-field exposure. Given the high number density of background sources, the profile has a much smaller scatter with respect to the case in which we consider the complete shear field. We tested this for the halo-4 at $z = 0.22$ and $z = 0.94$, generating 10,000 random shear field realisations, finding results consistent with our reference case well within $1\,\sigma$ of the credibility regions of the posteriors.

From the two components of the shear, we define the tangential shear $\gamma_{\rm t}$ (Umetsu 2020) at each sampled point θ_i of the map, as:

$$\gamma_{\rm t}(\theta_i) = -\gamma_1(x_i, y_i)\cos(2\phi_i) - \gamma_2(x_i, y_i)\sin(2\phi_i)\,, \tag{10}$$

where $(0, 0)$ is the centre of the cluster by construction, $\theta_i = (x_i^2 + y_i^2)^{1/2}$ and $\phi_i = \arctan(y_i/x_i)$. This gives us the possibility to write the excess surface mass density – azimuthally averaging the measured quantities – as:

$$\Delta\Sigma(\theta) = \bar{\Sigma}(<\theta) - \Sigma(\theta) \equiv \Sigma_{\rm crit}\gamma_{\rm t}(\theta)\,, \tag{11}$$

where $\Sigma(\theta)$ represents the mass surface density of the lens at distance θ from the putative cluster centre, and $\bar{\Sigma}(<\theta)$ its mean within θ.

The approach that we follow in this work aims at quantifying the weak lensing mass bias associated with projection effects and its redshift evolution, depending on the available number density of galaxies from which we can measure the lensing signal induced by the interposed cluster projected mass density distribution. In this way, we quantify the most optimistic weak lensing mass bias that we expect from *Euclid* data. In this analysis, we do not assume any uncertainty on the cluster centre, the lens and source redshifts, all assumed to be known with infinite accuracy. Forthcoming analyses, within the Euclid Collaboration,

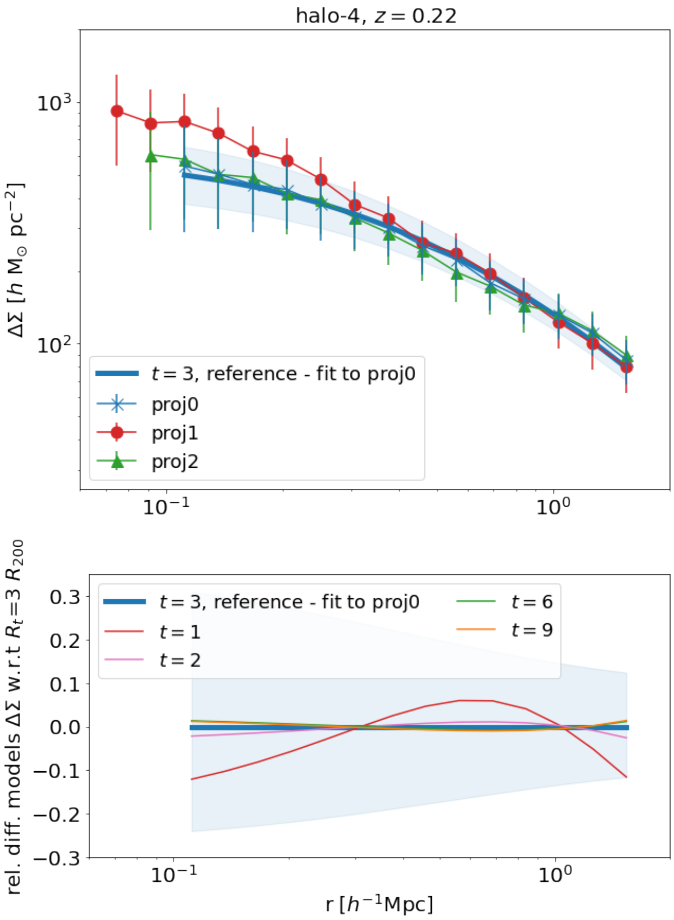

Fig. 4. *Top panel*: Excess surface mass density profiles of the three random projections for a cluster-size halo at $z_l = 0.22$, as displayed in Fig. 3. The blue, red and green data points show the circular averaged profiles of the halo projected along the z, y, and x axis of the re-simulation box. The error bars on the data points account for both the dispersion of the intrinsic ellipticity of background galaxies and the error associated with the average measure in the considered radial bin. The blue solid line displays the best-fit model to proj0, while the shaded region represents the model within the 68% of confidence. *Bottom panel*: relative difference of the best-fit models assuming different values of the truncation radius R_t with respect to the reference case with $t = 3$.

will be dedicated to study these systematics, and the corresponding propagation, into the weak lensing mass biases, and concentration that should be degenerate and more affected by the miscentring (Giocoli et al. 2021; Lesci et al. 2022).

To simulate the weak lensing signal of each cluster, we build the average excess surface mass density by binning the measured $\Delta\Sigma(r_i)$, where $r_i \equiv D_l\,\theta_i$, in 22 logarithmically equispaced intervals from 0.02 to 1.7 h^{-1} Mpc from the cluster centre. As an example, in the top panel of Fig. 4, blue, red, and green data points display the simulated $\Delta\Sigma$ profile for three random projections of the cluster halo-4 at $z = 0.22$, as shown in Fig. 3. In order to limit the analysis to well-constrained shear estimates (depending on the angular binning and on the source density), we consider only radial bins with at least 10 simulated data measures. This guarantees a reliable estimate of the average signal and conservatively neglects bins close to the centre, where baryonic effects tend to steepen the profile. However, we have tested that considering radial bins with at least one galaxy does not alter the mass bias results of our work. The colours correspond to those used for the panel frame of Fig. 3. The corresponding error bars are computed as:

$$\sigma_{\Delta\Sigma} = \sqrt{\sigma^2_{\langle\Delta\Sigma\rangle} + \Sigma^2_{\rm crit}\frac{\sigma_e^2}{n_g\,\pi\left(\theta_2^2 - \theta_1^2\right)}}\,, \tag{12}$$

where $\sigma_e = 0.3$ (Hoekstra et al. 2004, 2011; Kilbinger 2015; Euclid Collaboration: Blanchard et al. 2020) is the dispersion of the shape of background source galaxies, and θ_1 and θ_2 are the lower and the upper bounds of the considered radial annulus. In our error budget, we also include the error of the mean estimated excess surface mass density in each radial interval $\sigma_{\langle\Delta\Sigma\rangle} = \sigma_{\rm rms}/\sqrt{n_{\rm g,ring}}$ – with $\sigma_{\rm rms}$ representing the $\Delta\Sigma$ root-mean-square:

$$\sigma_{\rm rms} = \sqrt{\sum_{i=1}^{n_{\rm g,ring}}\frac{\left(\Delta\Sigma_i - \langle\Delta\Sigma\rangle_{\rm ring}\right)^2}{n_{\rm g,ring}}} \tag{13}$$

$\langle\Delta\Sigma\rangle_{\rm ring}$ the average value, and $n_{\rm g,ring}$ the number of galaxies in each ring – in order to account for: the projected cluster triaxiality, correlated large-scale structures, and subhalo contribution in each annulus (Gruen et al. 2015, 2011; Umetsu et al. 2020). It is also worth mentioning that this term is negligible with respect to the one that accounts for the intrinsic shape noise. From the figure, we notice that while proj0 and proj2 are similar, proj1 shows a steepening toward the centre. This highlights that depending on which projection, structural properties recovered from weak lensing mass and concentration can be different from each other and even in contrast with respect to the three-dimensional ones. In the figure, we highlight that the data binning of the three projections have a different minimum scale because we exclude the rings with less than 10 galaxies.

4. Analytical models & results

In order to recover the weak lensing mass and concentration, we model the data of the excess surface mass density profile using projected analytical relations. We use the same strategy that is under development within the Euclid Consortium in the implementation of the dedicated processing function: the total density profile is constructed considering the signal coming from the central part of the cluster called the 1-halo term, and the one caused by correlated large-scale structures, named the 2-halo term. Methods based on non-parametric formalism (Clowe et al. 2004; Bradač et al. 2005; Bradač et al. 2006; Diego et al. 2007; Merten et al. 2009; Jauzac et al. 2012; Jullo et al. 2014; Niemiec et al. 2020) may give more accurate and precise mass reconstructions, but at the price of being slow and memory expensive, and in this way, hardly applicable to the very large statistics of clusters expected from *Euclid* photometric data (Sartoris et al. 2016; Euclid Collaboration: Adam et al. 2019).

For the cluster main halo, we adopt a smoothly-truncated NFW density profile (BMO, Baltz et al. 2009), defined as:

$$\rho_{\rm BMO}(r_{\rm 3D}|M_{200}, c_{200}, R_t) = \rho_{\rm NFW}(r_{\rm 3D}|M_{200}, c_{200})\left(\frac{R_t^2}{r_{\rm 3D}^2 + R_t^2}\right)^2\,, \tag{14}$$

with $R_t = t\,R_{200}$ with t defined as the truncation factor. For our reference model, following the results by Oguri & Hamana (2011), Bellagamba et al. (2019), and Giocoli et al. (2021) we will adopt a truncation radius $R_t = 3\,R_{200}$. The total mass enclosed within R_{200}, i.e., M_{200}, can be thought of as the normalisation of the model and as a mass-proxy of the true enclosed

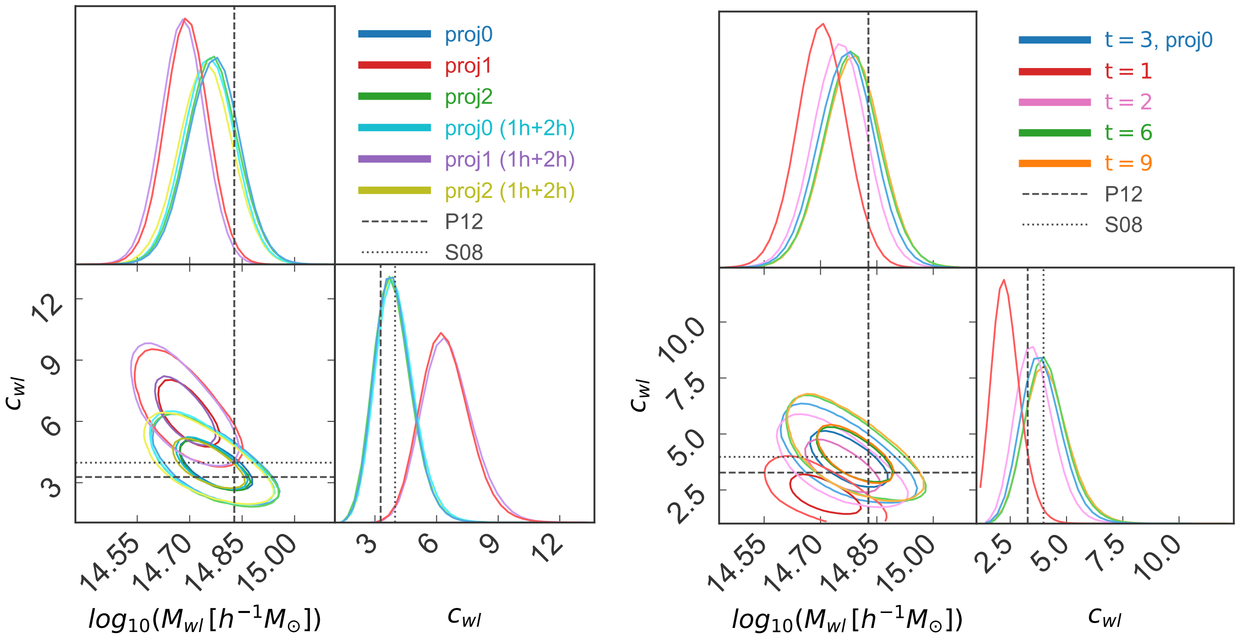

Fig. 5. *Left panel*: posterior distributions of the recovered logarithm of the mass $M_{\rm wl}$ and concentration $c_{\rm wl}$ obtained by fitting the excess surface mass density profile of the three random projections of the halo-4 at $z = 0.22$. *Right panel*: posterior distributions obtained modelling the excess surface mass density profile on the halo-4 when oriented along proj0, assuming different truncation radii. The blue data displays the reference case when assuming a truncation radius $R_{\rm t} = 3\,R_{200}$, while the red, pink, green and orange one exhibits the results when using $R_t = t\,R_{200}$ with $t = 1$, 2, 6, and 9, respectively. Dark and light-shaded areas enclose 1 and 3 σ credibility regions, respectively. In both panels the vertical dashed line marks the true mass of the system, while the horizontal dotted and dashed ones indicate the concentrations computed using the Springel et al. (2008a) and Prada et al. (2012) formalisms, respectively.

mass of the dark matter halo hosting the cluster (Giocoli et al. 2012a). Writing $r^2_{\rm 3D}$ as the sum in quadrature between the sky projected coordinate $D_{\rm d}\theta$ and the line-of-sight ζ coordinate, and integrating along ζ we can write

$$\Sigma_{\rm 1h}(\theta|M_{200}, c_{200}, R_{\rm t}) = \int_0^\infty \rho_{\rm BMO}(\theta, \zeta|M_{200}, c_{200}, R_{\rm t})\, {\rm d}\zeta\,. \quad (15)$$

This projected parametrisation describes the smooth blending of the halo boundary into the connected large-scale structures, regulated by the truncation radius. However, at larger distances from the cluster centre, the projected lensing signal starts to increase due to the large-scale structures of the correlated and the uncorrelated matter along the line of sight: the 2-halo term, describing the asymptotic regime far from the halo centre. This term can be written as a function of the integrated linear matter power spectrum weighted by a Bessel function (Oguri & Takada 2011; Oguri & Hamana 2011; Sereno et al. 2017),

$$\Delta\Sigma_{\rm 2h}(\theta, M_{200}) = \int_0^\infty \frac{\ell\, {\rm d}\ell}{2\pi} J_2(\ell\theta) \frac{\bar{\rho}_{\rm m}(z)\, b_{\rm h}(M_{200}; z_{\rm l})}{(1+z)^3 D_{\rm l}^2(z)} P_{\rm lin,m}(k_\ell; z_{\rm l})\,, \quad (16)$$

where $z_{\rm l}$ represents the cluster (lens) redshift, J_2 is the Bessel function of second type, $k_\ell = \ell/[(1+z)D_{\rm l}(z)]$ indicates the wave vector mode, $\bar{\rho}_{\rm m}$ is the background density, $P_{\rm lin,m}$ refers to the linear matter power spectrum and $b_{\rm h}(M; z)$ is the halo bias, for which we adopt the Tinker et al. (2010) model.

The total model can be read as follows:

$$\Delta\Sigma(\theta) = \Delta\Sigma_{\rm 1h}(\theta|M_{200}, c_{200}, R_{\rm t}) + \Delta\Sigma_{\rm 2h}(\theta, M_{200})\,. \quad (17)$$

It is worth noticing that the 2-halo term contribution at small radii is expected to be negligible, while its contribution becomes important, with respect to the 1-halo term, only at scales $\gtrsim 3\,h^{-1}$ Mpc (Giocoli et al. 2021; Ingoglia et al. 2022). In their Fig. 1, Giocoli et al. (2021) show that for distances between 2 and 3 h^{-1} Mpc from the halo centre the profile is sensitive also to the truncation radius definition. Given the size of the field-of-view of our maps, $3.4\,h^{-1}$ Mpc on a side, the 2-halo term has a weak contribution, and we decided to ignore it in our modelling function.

In the top panel of Fig. 4, the solid blue curve stands for the best-fit model to the data points of proj0, associated to the median values of the posteriors of $\log_{10}(M_{200})$ and c_{200}. The shaded region marks the 1 σ uncertainties of the recovered mass and concentration parameters propagating in the modelling of the $\Delta\Sigma$ profile, associated with the 16$^{\rm th}$ and 84$^{\rm th}$ percentiles of the posterior distributions. In the bottom panel, we show the relative difference of the best-fit models where adopting various values for the truncation radius with respect to the reference case where we set $R_{\rm t} = 3\,R_{200}$.

The left panel of Fig. 5 displays the posterior distributions of the recovered mass, $\log_{10}(M_{200})$, and concentration, c_{200}, obtained by modelling the three random projections of the halo-4 at $z_{\rm l} = 0.22$, (top panel of Fig. 4). In blue, red, and green, we show the distribution for the projections proj0, proj1, and proj2, respectively, using only the 1-halo term in our modelling function and fixing $R_{\rm t} = 3\,R_{200}$: we define this as the reference model.

We perform a Monte Carlo Markov Chain run assuming a Gaussian log-likelihood between the model and the data as defined within our reference CBL libraries[4] (Marulli et al. 2016) that can be read as:

$$\mathcal{L} \propto \exp\left(-\frac{1}{2}\chi^2\right)\,, \quad (18)$$

[4] https://gitlab.com/federicomarulli/CosmoBolognaLib

where

$$\chi^2 = \sum_i \left(\frac{\Delta\Sigma_i(\theta_i) - \Delta\Sigma_{\rm model}(\theta_i)}{\sigma_{\Delta\Sigma_i}} \right)^2 , \tag{19}$$

summing on the number of radial bins. Note that we do not account for reduced shear corrections both in the simulations and in the model; however, it is worth mentioning that observationally this model absorbs the reduced shear impact in the resulting mass bias. We set uniform priors for $\log_{10}(M_{200}/[h^{-1} M_\odot]) \in [12.5, 16]$ and $c_{200} \in [1, 15]$, and let each MCMC chain run for 16 000 steps. In cyan, purple, and gold, we show the posterior distributions obtained by also adding the contribution of the 2-halo term in the modelling function, as expressed by Eq. 16. Comparing the two, we notice that the results are in full agreement with the analysis that does not include the 2-halo term, also for high-redshift clusters. This guarantees that for each cluster and redshift the data-set that we built by projecting the mass density distribution from the simulations, takes a negligible contribution from correlated structures along the line-of-sight, due to the limited size of the field-of-view ($3.4\,h^{-1}$ Mpc), as discussed earlier.

In the right panel of Fig. 5, we examine the dependence of different assumptions for the truncation radius on the recovered weak lensing halo mass and concentration, as parametrised in Eq. 14 and inserted into Eq. 15. We show the posterior distributions when assuming t to be equal to 1 (red), 2 (pink), 3 (blue), 6 (green), and 9 (orange). From the figure, we notice that the different choices result in a diverse recovered concentration: smaller truncation radii prefer lower concentration parameters. When $t = 1$ (relatively unphysical case) and 2, the mass also tends to be underestimated. To guide the reader, we underline that in both panels the dotted and dashed lines refer to the true 3D halo mass and concentrations, adopting the Springel et al. (2008a) and Prada et al. (2012) relations, respectively.

In Fig. 6, we show the weak lensing mass bias as a function of the cluster true mass M_{200}, for systems at $z_l = 0.22$. The grey data points display the ratio between the weak lensing mass and the true mass, modelling the excess surface mass density profile with our reference model: 1-halo term with a truncation radius parameter $t = 3$. The error bars indicate the 16[th] and 84[th] percentiles of the posterior distributions for each considered cluster projection. The black solid line shows the moving average of the data. Red, pink, green, and orange lines display the moving average when considering the truncation radius equal to 1, 2, 6, and 9 times R_{200} in our modelling function, respectively (the corresponding data points are not displayed in the figure). From the figure, we notice that the average weak lensing cluster mass bias depends on the value of the truncation radius adopted in the modelling. In particular, assuming $t = 1$ we underestimate the mass by approximately $\sim 30\%$, larger t values increase the weak lensing mass and therefore decrease the mass bias. For our reference case with $t = 3$, the average mass bias is as low as $\sim 7\%$ with a standard deviation, shown by the grey shaded region (see also Becker & Kravtsov 2011), thus highlighting that triaxiality is the largest source of intrinsic scattering. The right panel exhibits the distributions for the corresponding cases independently of the halo mass M_{200}, while the top one shows the average relative uncertainty for the weak lensing mass estimates as a function of 3D cluster mass. The blue-filled circles report the results by Bahé et al. (2012, hereafter B12) that model the weak lensing mass bias using tangential shear profiles up to $2.2\,h^{-1}$ Mpc from the cluster centre (while we extend our analysis out to $1.7\ h^{-1}$ Mpc). Their value is larger than ours and the authors are using only the 1-halo term, modelled with a pure NFW profile (we adopt a truncated NFW using the BMO relation), without quantifying the 2-halo contribution – that, in their case, may not be entirely negligible because of a larger field of view. In addition, they use a dispersion parameter of the intrinsic shape of background source galaxies $\sigma_e = 0.2$ while we adopt a larger value $\sigma_e = 0.3$. All these factors may increase the relative uncertainties in the recovered weak lensing masses.

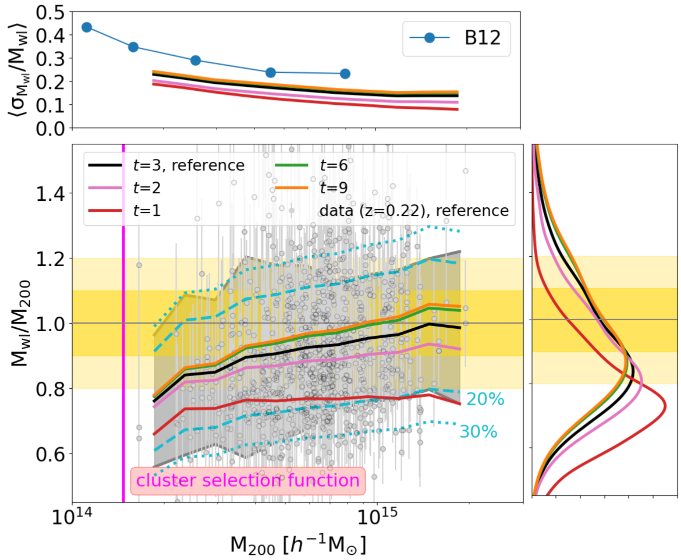

Fig. 6. Weak lensing mass bias as a function of the cluster true mass, for all systems at $z_l = 0.22$, for different assumptions of the truncation factor. The data points show the ratio between the recovered weak lensing mass obtained by fitting the excess surface mass density profile using our reference model – 1-halo term assuming a truncation radius $R_t = 3\,R_{200}$ – and the true M_{200} mass. The error bars correspond to the 16[th] and 84[th] percentiles of the posterior distribution. The black solid line represents the moving average of the data points. Red, pink, green, and orange lines display the moving average of the data considering the truncation radius parameter equal to $t = 1$, 2, 6, and 9 in our modelling function, respectively. The cyan dashed, and dotted lines point to 20 and 30% of the scatter, respectively, while the magenta vertical line indicates the minimum cluster mass – almost constant with redshift – expected to be detected from the photometric catalogue as predicted by Sartoris et al. (2016). The light and dark yellow bands mark 10% and 20% scatters, respectively. The top subpanel displays the relative weak lensing mass uncertainty as a function of the true cluster mass. The blue circles show the prediction by Bahé et al. (2012, hereafter B12). The histograms in the right panel show the weak lensing mass bias distributions over all cluster masses for the various considered cases.

4.1. Mass bias and concentration

In the spirit of understanding how well we can recover the weak lensing mass bias when assuming a concentration model, in Fig. 7 we show the posterior distribution of the logarithm of the recovered cluster mass in the case of the halo-4 when considering different assumptions for the concentration. Generally, we see they have an impact on the recovered mass. In particular, if we assume a fixed value equal to $c_{200} = 3$, we have no bias on the recovered mass for this specific cluster and projection. More relevant than mass biases for individual realisations are average biases computed for representative cluster samples, which show a similar dependence on the adopted concentration mass relation (e.g Sommer et al. 2022).

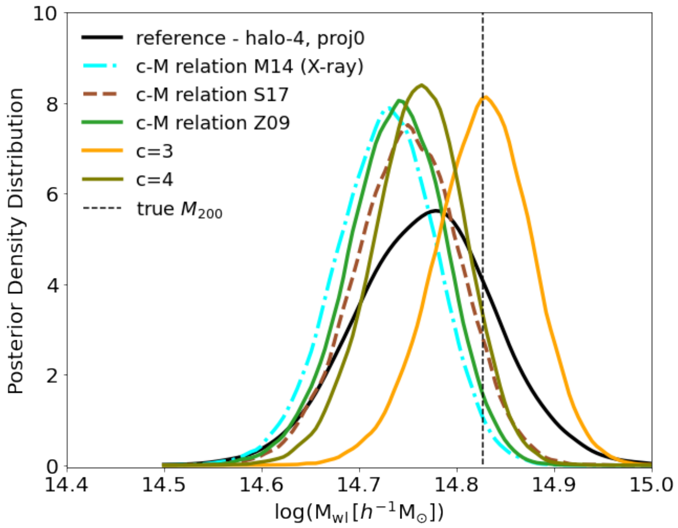

Fig. 7. Posterior distributions when recovering the logarithm of the cluster mass for proj0 of the halo-4 at $z = 0.22$. The black curve shows the reference case where we model both the mass and the concentration, as in the top panel of Fig. 5. The other histograms show the posteriors when assuming a parametrisation of the concentration-mass relation; in particular, orange and olive curves refer to the cases when assuming a constant value of $c_{200} = 3$ and $c_{200} = 4$, respectively. The vertical black dashed line marks the true value of M_{200} as computed by `AHF`.

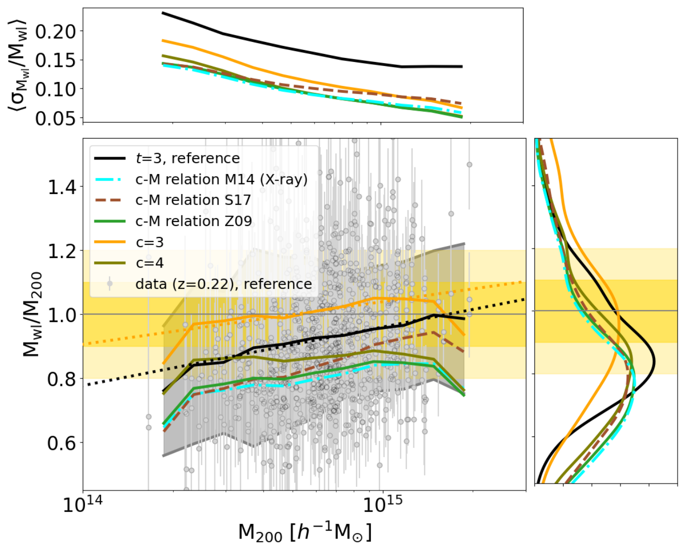

Fig. 8. Weak lensing mass biases for clusters at $z = 0.22$; the points are the same as in Fig. 6. The different line styles and coloured curves display the moving averages when assuming different approaches when modelling the concentration. The black solid line refers to the reference case where we vary both the mass and the concentration in our MCMC analysis. The solid green, dotted cyan, and dark-red curves refer to the case in which we assume a concentration-mass relation model, as in the figure label. On the other side, the orange and olive ones assume a constant value of $c_{200} = 3$ and $c_{200} = 4$, respectively. The coloured dotted lines display the linear regressions to the moving average and the corresponding uncertainty (not shown for the orange data to not overcrowd the figure). Top and left panels show the mean relative mass uncertainties as a function of the true cluster mass and the distributions of the weak lensing mass biases, respectively.

The average weak lensing mass bias, as a function of the true cluster mass, is displayed in Fig. 8. The black line shows our reference case. The solid green, dashed cyan, and dark red lines correspond to the moving average when assuming different concentration-mass relation models: Zhao et al. (2009), Meneghetti et al. (2014) and Sereno et al. (2017), respectively. The orange and olive curves display the results assuming a fixed value $c_{200} = 3$ and $c_{200} = 4$, respectively. Referring to the P12 (S08) model the average concentration of clusters at $z = 0.22$ is $\langle c_{200}\rangle = 4$ (5) (see the left panel of Fig. 1). The corresponding coloured dotted lines display the linear regressions:

$$\left\langle \frac{M_{wl}}{M_{200}} \right\rangle = \alpha \left\langle \log\left(\frac{M_{200}}{M_{14.5}}\right)\right\rangle + \beta\,, \quad (20)$$

where $M_{14.5} = 10^{14.5}\,h^{-1}M_\odot$, for the reference and $c_{200} = 3$ cases (see Tab. 3). The average values are computed assuming a step-size=0.1 and bin-size=0.3 in $\log(M_{200})$.

From the top subpanel, it is interesting to notice that the average relative scatter as a function of M_{200} is reduced by approximately a factor of two when assuming a deterministic model for the concentration, with respect to the case in which we vary it inside the Monte Carlo analyses. The right panel displays the distribution of the relative mass ratio.

4.2. Mass bias and relaxation criteria

The morphological properties of galaxy clusters depend on their mass assembly history. Typically, clusters that experienced recent merging events may contain a larger fraction of their mass in substructures and eventually a mass centroid which is not coincident with the position of the density peak due to the presence of multi-mass components. These properties manifest themselves in a variety of observables at different wavelengths, going from X-ray to the radio band. The projected mass recovered using weak lensing data is also influenced by the level of dynamical relaxation of the lens. In this section, we aim at quantifying these dependencies.

In the left panel of Fig. 9 we display the scatter plot of clusters at $z = 0.22$ for parameters f_{sub} and x_{off}, that we use to define the relaxation status of a system – see their definition in Sect. 2. We define as relaxed systems those with $f_{sub} < 0.1$ and $x_{off} < 0.05\,R_{200}$, i.e., the clusters lying in the lower left white rectangle of the figure: 147 over 324 objects satisfy this condition. Our relaxed clusters are green-circled, while unrelaxed systems are displayed using magenta circles. In the figure, we also mark the relaxation criterium adopted by Cui et al. (2018): $x_{off} < 0.04\,R_{200}$ (with a dotted vertical line) and with virial ratio $0.85 < \eta < 1.15$. The latter condition is portrayed in the figure, colouring the data points in blue or otherwise in yellow. The relation criterion adopted by Cui et al. (2018) is satisfied by 91 systems. In the right panel, we display the weak lensing mass bias, as a function of the cluster mass, for the relaxed (green) and the unrelaxed (magenta) clusters. The green and magenta solid curves represent the moving average of the two samples, respectively. The corresponding dashed curves refer to the cases in which the relaxation criterion by Cui et al. (2018) is adopted, which also uses information on the virial energy ratio. From the top subpanel, we notice that the average relative uncertainty in the recovered mass is lower for relaxed systems – even if the differences between the two cases are, to some extent, small, as well as the relative mass bias has a lower scatter than for unrelaxed clusters (right subpanel). This highlights the fact that unrelaxed systems could not be well modelled by the single halo model (Lee et al. 2023). As in previous figures, and to highlight the differences between the relaxed and unrelaxed samples, the

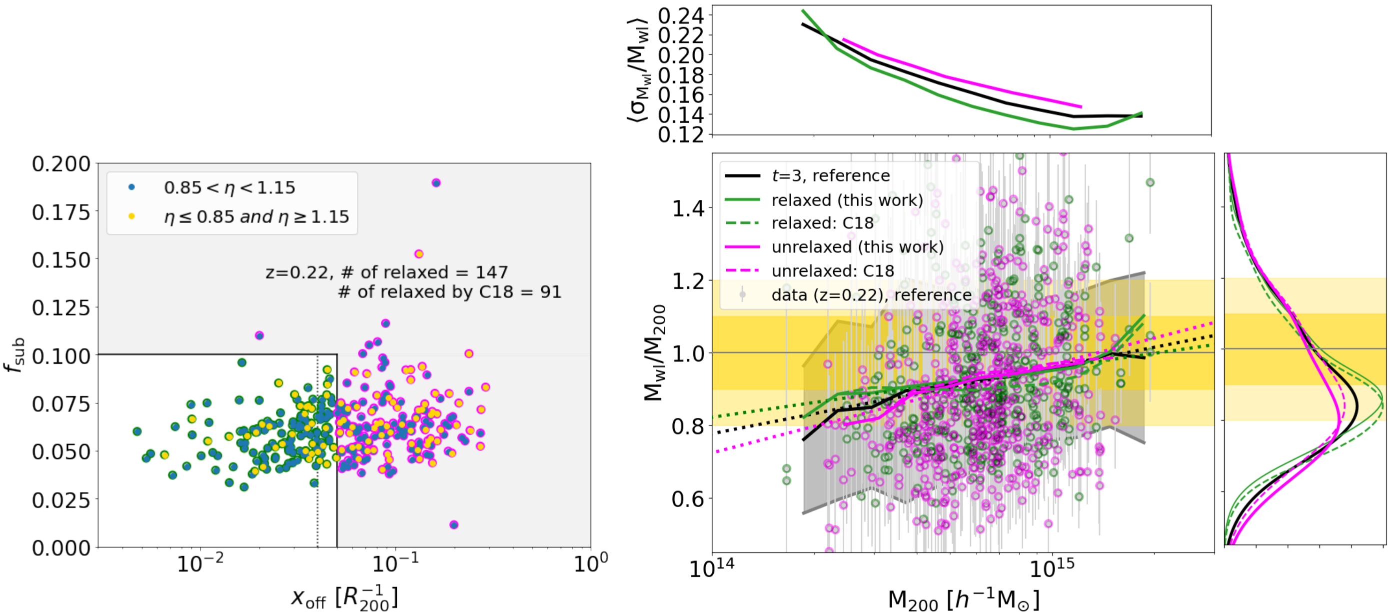

Fig. 9. *Left panel*: relaxation criteria for the clusters at $z = 0.22$. In our analysis, we assume the systems to be relaxed if their mass fraction in substructures $f_{\rm sub} < 0.1$ and their centre of mass offset $x_{\rm off} < 0.05\ R_{200}$ indicated by the white rectangular region on the bottom left. Our relaxed (unrelaxed) clusters are circled in green (purple). For comparison, we mark also the relaxation criterium by Cui et al. (2018): $f_{\rm sub} < 0.1$, $x_{\rm off} < 0.04\ R_{200}$ and energy parameter $0.85 < \eta < 1.15$ (blue-filled circle, otherwise gold-coloured). *Right panel*: weak lensing mass bias as a function of the true mass of the cluster. Green and magenta circled data points correspond to systems that are or are not relaxed, respectively; the solid green and magenta show the moving average of the two samples. For comparison, the dashed lines, accordingly coloured, show the results using the relaxation criteria by Cui et al. (2018). The sub-panel on the right displays the mass bias distributions for the various cluster samples, while the top one is the average relative scatter in the weak lensing mass estimates as a function of M_{200}.

coloured dotted lines display the linear regressions to the moving average and the corresponding uncertainty. The best-fit parameters and the corresponding uncertainties, as expressed in Eq. (20) for the relaxed and unrelaxed sample at $z = 0.22$ are shown in Tab. 2, which can be compared with the full sample as in Tab. 3.

Table 2. Linear regression parameters, as in Eq. (20), for the relaxed and unrelaxed cluster sample at $z = 0.22$.

	Slope α	Intercept β
relaxed	0.1354 ± 0.029	0.890 ± 0.596
unrelaxed	0.243 ± 0.033	0.846 ± 0.681

4.3. Mass bias along preferential directions

The reliability with which the cluster mass can be recovered is also related to the orientation of the moment of inertia tensor ellipsoid with respect to the line-of-sight (Sereno & Zitrin 2012; Sereno et al. 2013; Despali et al. 2014, 2017; Sereno et al. 2018). Herbonnet et al. (2022) have shown that the shape of the bright central galaxy can give unbiased information about the shape of the total halo mass ellipsoid and that the recovered mass via weak gravitational lensing is biased low (high) if the halo is oriented along the minor (major) axis with respect to the observer. In this section, we quantify in detail how the mass bias depends on the orientation of the mass tensor ellipsoid with respect to the line of sight. Following Sereno et al. (2017) and Umetsu et al. (2020), we can define the weak lensing signal-to-noise ratio as:

$$\frac{S}{N} = \frac{\dfrac{\sum_i \Delta\Sigma_i\, \sigma^{-2}_{\Delta\Sigma_i}}{\sum_i \sigma^{-2}_{\Delta\Sigma_i}}}{\left(\sum_i \sigma^{-2}_{\Delta\Sigma_i}\right)^{-1/2}}\,, \tag{21}$$

where the variable i runs on all the considered radial bins.

In the left panel of Fig. 10, we show the weak lensing signal-to-noise ratio of clusters at $z = 0.22$. The grey histogram shows the distribution of the S/N for all considered random projections, while the black curve displays the Kernel Density Estimate (KDE) of the binned histogram. Blue (dashed), red (dotted), and green (dot-dashed) curves refer to the distributions of the weak lensing signal-to-noise ratios when cluster ellipsoids are oriented with respect to the minor, intermediate, and major axis of the mass tensor ellipsoid. The triaxial parameters used are those computed by the AHF algorithm; we refer to Knollmann & Knebe (2009) and Cui et al. (2018) for more details. The results confirm that orientation matters: weak lensing signal-to-noise ratio distributions are shifted toward larger (lower) values when clusters are oriented along the major (minor) axis of the mass tensor ellipsoid with the line of sight. Projection effects also impact the weak lensing mass bias and the scatter, as we can observe in the right panel of Fig. 10. The mass bias, if clusters are preferentially selected either along the line of sight or in the plane of the sky, is approximately +25% or −25%. From the top subpanel, we can also notice that the average relative weak lensing mass uncertainty varies with the cluster ellipsoid orientation.

Before concluding this section, it is worth devoting a few words to cluster detections and orientation biases. At fixed mass, when systems are oriented along the major axis of the ellip-

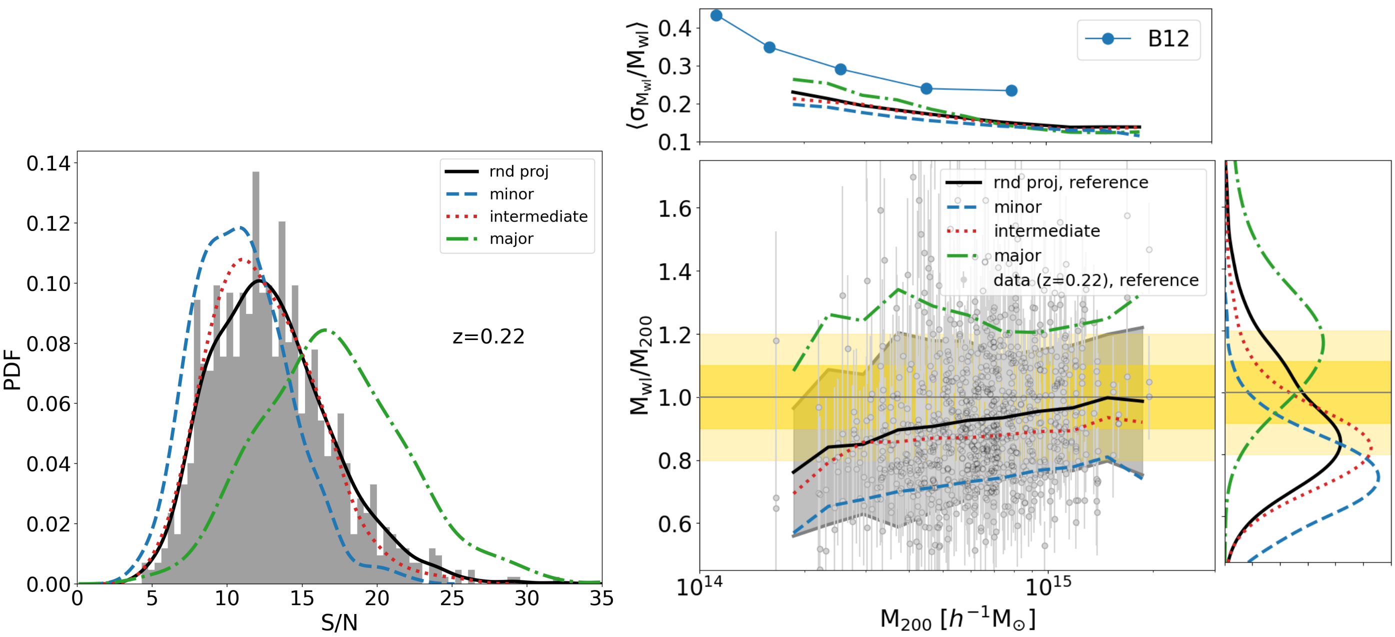

Fig. 10. *Left panel*: weak lensing signal-to-noise distributions for the sample of clusters at $z = 0.22$. The grey-shaded histogram shows the distribution for the clusters oriented along random projections, namely the x, y, and z cartesian axes of the re-stimulated box region. The solid black curve represents the Kernel Density Estimate (KDE) of the grey discrete histogram. The blue (dashed), red (dotted), and green (dot-dashed) curves refer to the KDE of the distributions when systems are oriented along the minor, intermediate, and major axis of the cluster ellipsoid, respectively. *Right panel*: weak lensing derived mass bias as a function of the true mass of the cluster. Blue (dashed), red (dotted), and green (dot-dashed) solid lines display the moving average of the corresponding mass bias data points of the preferential projections, minor, intermediate, and major axis, respectively. The top and right sub-panels display the relative mass uncertainties as a function of the true mass, and weak lensing mass bias distributions, respectively.

soid, they tend to have, on average, a more compact and concentrated galaxy satellite distribution than when they are oriented along the minor axis: this indicates that optical cluster finder algorithms in observational data may suffer from orientation bias (Wu et al. 2022). We plan to examine and analyse this argument in more detail in a future dedicated work.

For example, in Fig. 11, the magenta solid curve shows the average excess surface mass density profile of the 6 projections of cluster halo-4 at redshift $z = 0.22$. Solid red, blue, and green lines are the individual profiles for three random projections. Dotted blue, orange, and green curves show the profiles when the cluster is oriented along the minor, intermediate, and major axis of the ellipsoid, with respect to the line of sight, as done previously. Only radial bins with more than 10 galaxies are shown.

4.4. Reshift evolution of the mass bias

The expected source redshift distribution available for weak lensing measurements tells us how many background sources can be used to probe the total projected mass distribution of a cluster acting as a gravitational lens. The reliability of the lensing measurement also depends on the intrinsic magnitude of the sources and their projected distance with respect to the cluster centre because of possible confusion with cluster member galaxies. The weak lensing signal-to-noise ratio of individual clusters is also modulated by the expected available number density of sources expected from the *Euclid* wide survey, as we display in Fig. 12. Low-redshift systems have a larger weak lensing signal-to-noise ratio than the high-redshift ones. In the figure, we consider only the measurement of the three random projections per cluster since we have already discussed in the previous section that the three preferential ones need particular attention.

We also underline that eventual stacking procedures will shift the expected weak lensing signal-to-noise ratio distributions toward larger values by a factor that is approximately equal to the square root of the number of systems that are combined.

In Fig. 13 we exhibit the average weak lensing mass bias for the different redshifts, considering the three random projections per cluster, and cluster masses with $M_{200} > 10^{14} M_{\odot}$. In our modelling analysis, we assume a uniform range both for the logarithm of the mass and for the concentration parameter. On average, higher redshift clusters tend to be more biased low with respect to M_{200}, as a result of their lower signal-to-noise ratio. Looking to the top subpanel, it is interesting to notice that the relative error of the recovered weak lensing mass tends to be larger for systems at higher redshifts, which is due to the lower background source densities and average lensing efficiencies for those systems. In Tab. 3 we summarise the values of the parameters describing the linear fitting functions and the corresponding uncertainties, as in Eq. (20), at different redshifts, for the reference modelling case, and assuming a constant concentration $c_{200} = 3$.

Averaging over all cluster masses with $M_{200} > 10^{14} M_{\odot}$, we display in Fig. 14 the weak lensing mass bias as a function of the lens redshift. Black circles show the results averaged over all random projections. We can notice that higher redshift systems are more biased low with respect to the low redshift ones. Blue crosses and green squares represent the redshift evolution of the mass bias when the clusters are oriented along the minor or major axis of the ellipsoid with respect to the line of sight, respectively. Orange diamonds and olive pentagons refer to the case when in individual random projections, we model only the logarithm of the cluster mass while keeping the concentration fixed to $c_{200} = 3$ and $c_{200} = 4$, respectively. Those values represent

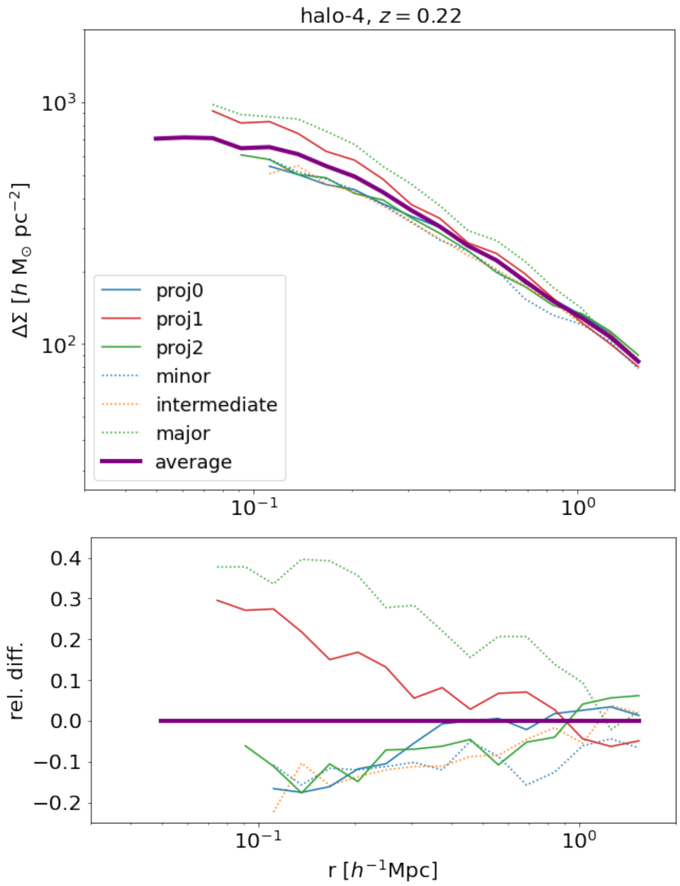

Fig. 11. *Top panel*: average excess surface mass density profile averaging six different projections of the same cluster (halo-4 at $z = 0.22$): three randoms and three preferentials. For comparison, solid blue, red, and green curves show the individual profiles around the three random projections, while dashed blue, orange and green when the cluster is oriented along the minor, intermediate and major axis of the moment of inertia tensor ellipsoid. *Bottom panel*: relative difference of the individual profiles with respect to the averaged one.

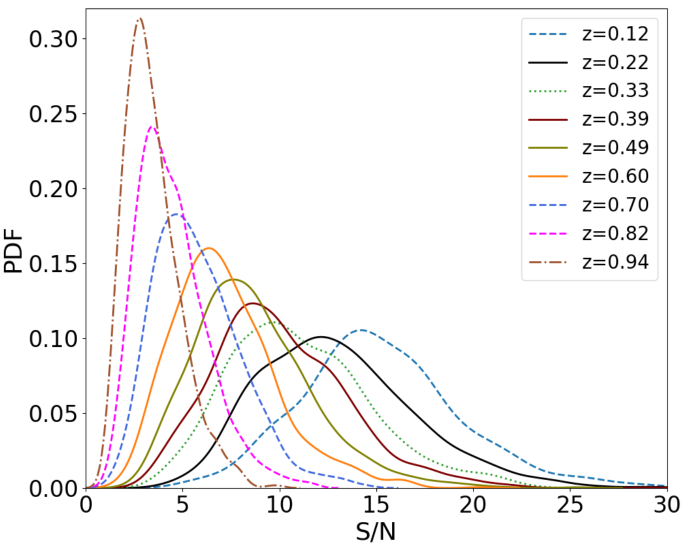

Fig. 12. Individual cluster weak lensing signal-to-noise ratio distributions, for random projections and different redshifts, as expected in the *Euclid* wide-field survey of a cluster population that is representative of the simulated clusters studied here.

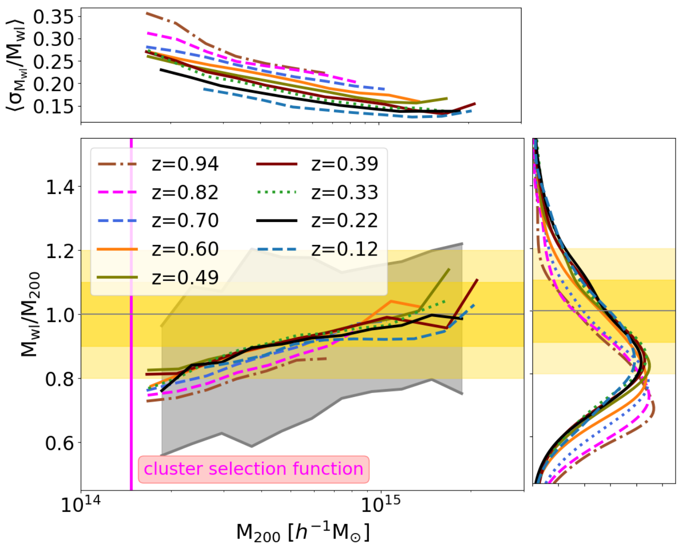

Fig. 13. Average weak lensing mass bias as a function of the cluster halo mass M_{200} for different lens redshifts. We consider all clusters with $M_{200} > 10^{14} M_\odot$, above the minimum mass expected to be selected in the photometric catalogue (Sartoris et al. 2016), relatively constant with redshift. Right and top subpanels are the same as Fig. 6.

the typical concentration parameters of cluster size-halo as highlighted in different numerical simulation analyses (Zhao et al. 2009; Giocoli et al. 2012b; Ludlow et al. 2012, 2016). Assuming a fixed concentration $c_{200} = 3$ in our modelling analysis of the weak lensing signal of individual clusters, we can recover, on average, a weak lensing mass that is biased by no more than 5% with respect to the true one, up to redshift $z = 0.7$ – positive for $z < 0.4$ and negative at higher redshift. The error bars associated with all data points correspond to the errors on the mean value. The dotted lines, which differ more significantly from each other at $z > 0.6$, display the results for the whole cluster sample with no minimum mass cut.

Table 3. Linear regression parameters as in Eq. (20), at different redshifts for the reference and $c_{200} = 3$ cases, considering random projections and for clusters more massive than $M_{200} > 10^{14} M_\odot$.

snap.	z	Slope α	Intercept β
reference	0.12	0.090 ± 0.028	0.883 ± 0.598
$c_{200} = 3$	"	-0.017 ± 0.035	1.053 ± 0.736
	0.22	0.183 ± 0.022	0.869 ± 0.452
	"	0.133 ± 0.027	0.973 ± 0.567
	0.33	0.208 ± 0.023	0.874 ± 0.473
	"	0.196 ± 0.025	0.966 ± 0.524
	0.39	0.215 ± 0.022	0.873 ± 0.464
	"	0.142 ± 0.027	0.974 ± 0.549
	0.49	0.223 ± 0.022	0.874 ± 0.453
	"	0.064 ± 0.024	0.985 ± 0.501
	0.59	0.273 ± 0.019	0.862 ± 0.401
	"	0.126 ± 0.024	0.976 ± 0.486
	0.70	0.292 ± 0.024	0.836 ± 0.488
	"	0.172 ± 0.027	0.951 ± 0.556
	0.82	0.279 ± 0.023	0.811 ± 0.473
	"	0.218 ± 0.028	0.935 ± 0.564
	0.94	0.255 ± 0.024	0.790 ± 0.498
	"	0.314 ± 0.032	0.920 ± 0.653

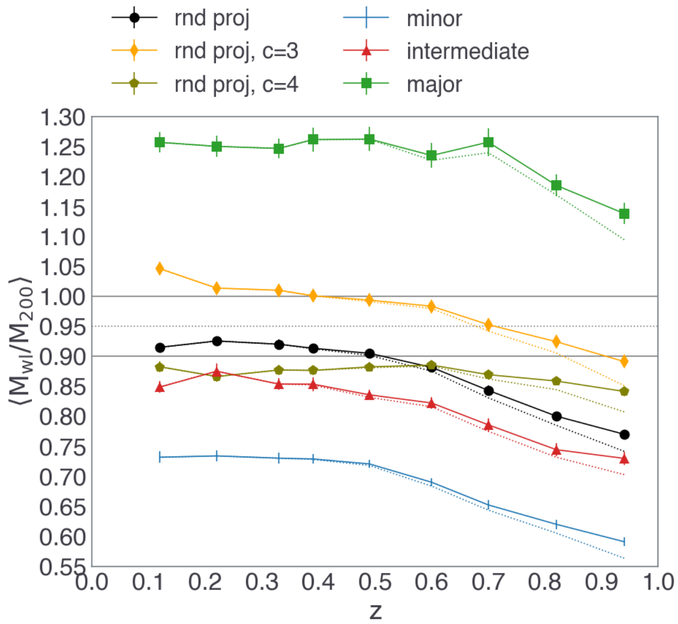

Fig. 14. Average cluster weak lensing mass bias as a function of the lens redshift, for clusters with $M_{200} > 10^{14} M_{\odot}$. The various data points and colours refer to different ways of computing the cluster masses. Black circles display the case of random projections and modelling both the halo mass and concentration, orange diamonds, and olive-coloured pentagons consider the cases in which we assume a fixed concentration parameter – three and four, respectively – and we fit only the halo mass. Light-blue crosses, red triangles and green squares show the average mass bias for the three particular projections, along the minor, the intermediate, and the major axis, respectively. The dotted lines, which slightly deviated from the data points only at $z > 0.6$, correspond to the results for the whole cluster sample, with no minimum mass cut.

The impact of the scatter and the redshift evolution of the cluster mass bias will be of utter importance for cluster cosmology. Different future works have already been planned and organised to further assess systematics and nuisance parameters in the cosmological likelihood pipeline.

5. Summary & Conclusions

In this work, we have performed a systematic study of the weak lensing mass bias using hydrodynamical simulations of clusters. We have simulated the expected excess surface mass density profile from the expected number density of background sources of the ESA *Euclid* wide-field survey, normalised to 30 galaxies per square arcminute. We have adopted a projected truncated NFW profile to model the data. Our main results are summarised as follows:

- on average individual weak lensing masses $M_{\rm wl}$ are typically lower by 5% than the true one, various projections of the same cluster may have different recovered weak lensing masses differing by up to 30%: cluster triaxiality represents the largest source of intrinsic scattering;
- in our reference model, we have adopted a truncation radius of three times R_{200}, a lower truncation radius returns a more biased weak-lensing mass: from $t = 1$ to $t = 9$ the mass bias for clusters at $z = 0.22$ ranges from -30% to a few percent;
- in modelling the data set we have also investigated the impact of using a concentration both dependent, in one case, and independent of the total mass in another case, finding that those systematically impact the recovered weak lensing mass (see e.g. also Sommer et al. 2022);
- relaxed clusters, being better described by a 1-halo projected density profile are less biased than the unrelaxed ones by approximately 3%;
- clusters oriented along the major (minor) axis of the mass tensor ellipsoid have their weak lensing mass overestimated (underestimated) by approximately $+(-)$ 25%;
- averaging over all masses, when also varying the concentration, the negative mass bias tends to increase as a function of redshift; however, assuming a fixed concentration, this effect is reduced. The increase of the negative mass bias with redshift is due to the reduced S/N of the weak lensing mass constraints of high-redshift clusters. As demonstrated by Sommer et al. (2022) this S/N dependence can be avoided if the weak lensing mass scatter is separated into an intrinsic component (e.g. due to variations in density profiles and substructures) and a shape noise component (e.g. Bocquet et al. 2019; Chiu et al. 2022).

The use of galaxy clusters as cosmological probes relies on the accuracy and precision of mass measurements. The future ESA *Euclid* mission will make use of weak gravitational lensing to determine the projected total mass. In this work, we have quantified the accuracy and bias effects by using dedicated lensing simulations of clusters in a variety of dynamical states and at different redshifts, based on a specific set of hydrodynamical simulations: the Three Hundred clusters. While the mass bias depends on the considered choice of the modelling function, the scatter is driven by the complex triaxial structure of galaxy clusters. However, assuming a fixed value $c_{200} = 3$ for the concentration parameter, when modelling the data of individual clusters, produces less unbiased results, at least for the set of simulated clusters analysed in this work.

We would like to conclude underling that future works will be devoted to study whether these calibrations are robust against variations in the astrophysical processes included in the simulations, paving the way for future cluster analyses and opening new perspectives for the cosmological exploitation of galaxy clusters.

Acknowledgements. CG, MM, and LM acknowledge support from the grant PRIN-MIUR 2017 WSCC32 ZOOMING, and the support from the grant ASI n.2018-23-HH.0. CG acknowledges funding from the Italian National Institute of Astrophysics under the grant "Bando PrIN 2019", PI: Viola Allevato and from the HPC-Europa3 Transnational Access programme HPC17VDILO. GC also thanks the support from INAF theory Grant 2022: Illuminating Dark Matter using Weak Lensing by Cluster Satellites, PI: Carlo Giocoli. MM acknowledge financial support from PRIN-MIUR grant and 2020SKSTHZ, INAF "main-stream" 1.05.01.86.20: "Deep and wide view of galaxy clusters (P.I.: M. Nonino)" and INAF "main-stream" 1.05.01.86.31 "The deepest view of high-redshift galaxies and globular cluster precursors in the early Universe" (P.I.: E. Vanzella). SB and MM acknowledge financial support from the InDark INFN Grant. GY and AK would like to thank the Ministerio de Ciencia e Innovación (Spain) for financial support under research grant PID2021-122603NB-C21 The THREE HUNDRED simulations used in this work have been performed in the MareNostrum Supercomputer at the Barcelona Supercomputing Center, thanks to CPU time granted by the Red Española de Supercomputación. WC is supported by the STFC AGP Grant ST/V000594/1 and the Atracción de Talento Contract no. 2020-T1/TIC-19882 granted by the Comunidad de Madrid in Spain. He also thanks the Ministerio de Ciencia e Innovación (Spain) for financial support under Project grant PID2021-122603NB-C21. He further acknowledges the science research grants from the China Manned Space Project with NO. CMS-CSST-2021-A01 and CMS-CSST-2021-B01. We acknowledge the use of computational resources from the parallel computing cluster of the Open Physics Hub (https://site.unibo.it/openphysicshub/en) at the Physics and Astronomy Department in Bologna. TS acknowledges support from FFG grant number 899537. CJM acknowledges FCT and POCH/FSE (EC) support through Investigador FCT Contract 2021.01214.CEECIND/CP1658/CT0001. The figures with the corner plots displaying the posterior distributions have been produced using the package `pygtc` developed by Bocquet & Carter (2016). The authors acknowledge the Euclid Consortium, the European Space Agency, and a number of agencies and institutes that have supported the development of *Euclid*, in particular the Academy of Finland, the Agenzia Spaziale Italiana, the Belgian Science Policy, the Canadian Euclid Consortium, the French Centre National d'Etudes Spatiales, the Deutsches Zentrum für Luft- und Raumfahrt, the Danish Space Research Institute, the Fundação para a Ciência e a Tecnologia, the Ministerio de Ciencia e Innovación, the National Aeronautics and Space Administration, the National Astronomical Observatory of Japan, the Netherlandse Onderzoekschool Voor Astronomie, the Norwegian Space Agency, the Romanian Space Agency, the State Secretariat for Education, Research and Innovation (SERI) at the Swiss Space Office (SSO), and the United Kingdom Space Agency. A complete and detailed list is available on the *Euclid* web site (`http://www.euclid-ec.org`).

References

Ahad, S. L., Bahé, Y. M., Hoekstra, H., van der Burg, R. F. J., & Muzzin, A. 2021, MNRAS, 504, 1999
Allen, S. W., Evrard, A. E., & Mantz, A. B. 2011, ARA&A, 49, 409
Angelinelli, M., Vazza, F., Giocoli, C., et al. 2020, MNRAS, 495, 864
Ansarifard, S., Rasia, E., Biffi, V., et al. 2020, A&A, 634, A113
Applegate, D. E., Mantz, A., Allen, S. W., et al. 2016, MNRAS, 457, 1522
Bahé, Y. M., McCarthy, I. G., & King, L. J. 2012, MNRAS, 421, 1073
Baltz, E. A., Marshall, P., & Oguri, M. 2009, J. Cosmology Astropart. Phys., 2009, 015
Barnes, D. J., Vogelsberger, M., Pearce, F. A., et al. 2021, MNRAS, 506, 2533
Bartelmann, M. 2010, Classical and Quantum Gravity, 27, 233001
Bartelmann, M. & Schneider, P. 2001, Physics Reports, 340, 291
Beck, A. M., Dolag, K., & Donnert, J. M. F. 2016, MNRAS, 458, 2080
Becker, M. R. & Kravtsov, A. V. 2011, ApJ, 740, 25
Bellagamba, F., Maturi, M., Hamana, T., et al. 2011, MNRAS, 413, 1145
Bellagamba, F., Roncarelli, M., Maturi, M., & Moscardini, L. 2018, MNRAS, 473, 5221
Bellagamba, F., Sereno, M., Roncarelli, M., et al. 2019, MNRAS, 484, 1598
Benitez-Llambay, A. 2015, py-sphviewer: Py-SPHViewer v1.0.0
Biffi, V., Borgani, S., Murante, G., et al. 2016, ApJ, 827, 112
Biviano, A., Murante, G., Borgani, S., et al. 2006, A&A, 456, 23
Biviano, A., Rosati, P., Balestra, I., et al. 2013, A&A, 558, A1
Bocquet, S. & Carter, F. W. 2016, The Journal of Open Source Software, 1
Bocquet, S., Dietrich, J. P., Schrabback, T., et al. 2019, ApJ, 878, 55
Bocquet, S., Heitmann, K., Habib, S., et al. 2020, ApJ, 901, 5
Bocquet, S., Saro, A., Dolag, K., & Mohr, J. J. 2016a, MNRAS, 456, 2361
Bocquet, S., Saro, A., Mohr, J. J., et al. 2015, ApJ, 799, 214
Bonamigo, M., Despali, G., Limousin, M., et al. 2015, MNRAS, 449, 3171
Bradač, M., Clowe, D., Gonzalez, A. H., et al. 2006, ApJ, 652, 937
Bradač, M., Schneider, P., Lombardi, M., & Erben, T. 2005, A&A, 437, 39
Capasso, R., Saro, A., Mohr, J. J., et al. 2019, MNRAS, 482, 1043
Castro, T., Borgani, S., Dolag, K., et al. 2021, MNRAS, 500, 2316
Chiu, I. N., Ghirardini, V., Liu, A., et al. 2022, A&A, 661, A11
Chua, K. T. E., Pillepich, A., Rodriguez-Gomez, V., et al. 2017, MNRAS, 472, 4343
Clowe, D., Gonzalez, A., & Markevitch, M. 2004, ApJ, 604, 596
Cromer, D., Battaglia, N., Miyatake, H., & Simet, M. 2022, J. Cosmology Astropart. Phys., 2022, 034
Cropper, M., Pottinger, S., Niemi, S., et al. 2016, in Society of Photo-Optical Instrumentation Engineers (SPIE) Conference Series, Vol. 9904, Space Telescopes and Instrumentation 2016: Optical, Infrared, and Millimeter Wave, ed. H. A. MacEwen, G. G. Fazio, M. Lystrup, N. Batalha, N. Siegler, & E. C. Tong, 99040Q
Cui, W., Dave, R., Knebe, A., et al. 2022, MNRAS, 514, 977
Cui, W., Knebe, A., Yepes, G., et al. 2018, MNRAS, 480, 2898
Cusworth, S. J., Kay, S. T., Battye, R. A., & Thomas, P. A. 2014, MNRAS, 439, 2485
Damsted, S., Finoguenov, A., Clerc, N., et al. 2023, arXiv e-prints, arXiv:2307.08749
De Lucia, G., Kauffmann, G., Springel, V., et al. 2004, MNRAS, 348, 333
Debackere, S. N. B., Hoekstra, H., & Schaye, J. 2022a, MNRAS, 515, 6023
Debackere, S. N. B., Hoekstra, H., Schaye, J., Heitmann, K., & Habib, S. 2022b, MNRAS, 515, 3383
Debackere, S. N. B., Schaye, J., & Hoekstra, H. 2021, MNRAS, 505, 593
Despali, G., Giocoli, C., Angulo, R. E., et al. 2016, MNRAS, 456, 2486
Despali, G., Giocoli, C., Bonamigo, M., Limousin, M., & Tormen, G. 2017, MNRAS, 466, 181
Despali, G., Giocoli, C., & Tormen, G. 2014, MNRAS, 443, 3208
Diego, J. M., Tegmark, M., Protopapas, P., & Sandvik, H. B. 2007, MNRAS, 375, 958
Dietrich, J. P., Bocquet, S., Schrabback, T., et al. 2019, MNRAS, 483, 2871
Ettori, S. & Eckert, D. 2022, A&A, 657, L1
Euclid Collaboration: Adam, R., Vannier, M., et al. 2019, A&A, 627, A23
Euclid Collaboration: Blanchard, A., Camera, S., et al. 2020, A&A, 642, A191
Euclid Collaboration: Castro, T., Fumagalli, A., et al. 2022, arXiv:2208.02174
Euclid Collaboration: Scaramella, R., Amiaux, J., et al. 2022, A&A, 662, A112
Gao, L., White, S. D. M., Jenkins, A., Stoehr, F., & Springel, V. 2004, MNRAS, 355, 819
Gianfagna, G., De Petris, M., Yepes, G., et al. 2021, MNRAS, 502, 5115
Giocoli, C., Marulli, F., Moscardini, L., et al. 2021, A&A, 653, A19
Giocoli, C., Meneghetti, M., Bartelmann, M., Moscardini, L., & Boldrin, M. 2012a, MNRAS, 421, 3343
Giocoli, C., Meneghetti, M., Ettori, S., & Moscardini, L. 2012, MNRAS, 426, 1558
Giocoli, C., Meneghetti, M., Metcalf, R. B., Ettori, S., & Moscardini, L. 2014, MNRAS, 440, 1899
Giocoli, C., Tormen, G., & Sheth, R. K. 2012b, MNRAS, 422, 185
Giocoli, C., Tormen, G., Sheth, R. K., & van den Bosch, F. C. 2010a, MNRAS, 404, 502
Giocoli, C., Tormen, G., & van den Bosch, F. C. 2008, MNRAS, 386, 2135
Gonzalez, A. 2014, in Building the Euclid Cluster Survey - Scientific Program, proceedings of a conference held July 6-11 2014 at the Sexten Center for Astrophysics., 7
Grandis, S., Bocquet, S., Mohr, J. J., Klein, M., & Dolag, K. 2021, MNRAS, 507, 5671
Grandis, S., Mohr, J. J., Dietrich, J. P., et al. 2019, MNRAS, 488, 2041
Gruen, D., Bernstein, G. M., Lam, T. Y., & Seitz, S. 2011, MNRAS, 416, 1392
Gruen, D., Seitz, S., Becker, M. R., Friedrich, O., & Mana, A. 2015, MNRAS, 449, 4264
Henson, M. A., Barnes, D. J., Kay, S. T., McCarthy, I. G., & Schaye, J. 2017, MNRAS, 465, 3361
Herbonnet, R., Crawford, A., Avestruz, C., et al. 2022, MNRAS, 513, 2178
Hoekstra, H. 2001, A&A, 370, 743
Hoekstra, H. 2003, MNRAS, 339, 1155
Hoekstra, H., Bartelmann, M., Dahle, H., et al. 2013, Space Sci. Rev., 177, 75
Hoekstra, H., Hartlap, J., Hilbert, S., & van Uitert, E. 2011, MNRAS, 412, 2095
Hoekstra, H., Yee, H. K. C., & Gladders, M. D. 2004, ApJ, 606, 67
Ingoglia, L., Covone, G., Sereno, M., et al. 2022, MNRAS, 511, 1484
Jauzac, M., Jullo, E., Kneib, J.-P., et al. 2012, MNRAS, 426, 3369
Jullo, E., Pires, S., Jauzac, M., & Kneib, J.-P. 2014, MNRAS, 437, 3969
Jung, S. L., Rennehan, D., Saeedzadeh, V., et al. 2022, MNRAS, 515, 22
Kiiveri, K., Gruen, D., Finoguenov, A., et al. 2021, MNRAS, 502, 1494
Kilbinger, M. 2015, Reports on Progress in Physics, 78, 086901
Klypin, A., Yepes, G., Gottlöber, S., Prada, F., & Heß, S. 2016, MNRAS, 457, 4340
Knollmann, S. R. & Knebe, A. 2009, ApJS, 182, 608
Kravtsov, A. V. & Borgani, S. 2012, ARA&A, 50, 353
Lau, E. T., Kravtsov, A. V., & Nagai, D. 2009, ApJ, 705, 1129
Laureijs, R., Amiaux, J., Arduini, S., et al. 2011, arXiv:1110.3193
Lee, W., Cha, S., Jee, M. J., et al. 2023, ApJ, 945, 71
Lesci, G. F., Marulli, F., Moscardini, L., et al. 2022, A&A, 659, A88
Ludlow, A. D., Bose, S., Angulo, R. E., et al. 2016, MNRAS, 460, 1214
Ludlow, A. D., Navarro, J. F., Li, M., et al. 2012, MNRAS, 427, 1322
Martizzi, D., Mohammed, I., Teyssier, R., & Moore, B. 2014, MNRAS, 440, 2290
Marulli, F., Veropalumbo, A., & Moresco, M. 2016, Astronomy and Computing, 14, 35
Maturi, M., Bellagamba, F., Radovich, M., et al. 2019, MNRAS, 485, 498
Meneghetti, M., Melchior, P., Grazian, A., et al. 2008, A&A, 482, 403
Meneghetti, M. & Rasia, E. 2013, arXiv:1303.6158
Meneghetti, M., Rasia, E., Merten, J., et al. 2010b, A&A, 514, A93
Meneghetti, M., Rasia, E., Vega, J., et al. 2014, ApJ, 797, 34
Merten, J., Cacciato, M., Meneghetti, M., Mignone, C., & Bartelmann, M. 2009, A&A, 500, 681
Mostoghiu, R., Knebe, A., Cui, W., et al. 2019, MNRAS, 483, 3390
Navarro, J. F., Frenk, C. S., & White, S. D. M. 1996, ApJ, 462, 563
Navarro, J. F., Frenk, C. S., & White, S. D. M. 1997, ApJ, 490, 493
Niemiec, A., Jauzac, M., Jullo, E., et al. 2020, MNRAS, 493, 3331
Oguri, M. & Hamana, T. 2011, MNRAS, 414, 1851
Oguri, M. & Takada, M. 2011, Phys. Rev. D, 83, 023008
Ondaro-Mallea, L., Angulo, R. E., Zennaro, M., Contreras, S., & Aricò, G. 2022, MNRAS, 509, 6077
Planck Collaboration. 2016, Astron. Astrophys., 594, A13
Planelles, S., Borgani, S., Fabjan, D., et al. 2014, MNRAS, 438, 195
Prada, F., Klypin, A. A., Cuesta, A. J., Betancort-Rijo, J. E., & Primack, J. 2012, MNRAS, 423, 3018
Pratt, G. W., Arnaud, M., Biviano, A., et al. 2019, Space Sci. Rev., 215, 25
Rasia, E., Borgani, S., Ettori, S., Mazzotta, P., & Meneghetti, M. 2013, ApJ, 776, 39
Rasia, E., Borgani, S., Murante, G., et al. 2015, ApJ, 813, L17
Rasia, E., Meneghetti, M., Martino, R., et al. 2012, New Journal of Physics, 14, 055018
Sartoris, B., Biviano, A., Fedeli, C., et al. 2016, MNRAS, 459, 1764
Schaller, M., Frenk, C. S., Bower, R. G., et al. 2015a, MNRAS, 451, 1247
Schaller, M., Frenk, C. S., Bower, R. G., et al. 2015b, MNRAS, 452, 343
Schrabback, T., Applegate, D., Dietrich, J. P., et al. 2018, MNRAS, 474, 2635
Schrabback, T., Bocquet, S., Sommer, M., et al. 2021, MNRAS, 505, 3923
Sereno, M., Covone, G., Izzo, L., et al. 2017, MNRAS, 472, 1946
Sereno, M., Ettori, S., Umetsu, K., & Baldi, A. 2013, MNRAS, 428, 2241
Sereno, M., Umetsu, K., Ettori, S., et al. 2018, ApJ, 860, L4
Sereno, M. & Zitrin, A. 2012, MNRAS, 419, 3280
Sheth, R. K. & Tormen, G. 1999, MNRAS, 308, 119
Simet, M., Battaglia, N., Mandelbaum, R., & Seljak, U. 2017a, MNRAS, 466, 3663
Simet, M., McClintock, T., Mandelbaum, R., et al. 2017b, MNRAS, 466, 3103
Sommer, M. W., Schrabback, T., Applegate, D. E., et al. 2022, MNRAS, 509, 1127

Springel, V. & Hernquist, L. 2003, MNRAS, 339, 289
Springel, V., Wang, J., Vogelsberger, M., et al. 2008a, MNRAS, 391, 1685
Springel, V., White, S. D. M., Frenk, C. S., et al. 2008b, Nature, 456, 73
Springel, V., White, S. D. M., Tormen, G., & Kauffmann, G. 2001, MNRAS, 328, 726
Steinborn, L. K., Dolag, K., Hirschmann, M., Prieto, M. A., & Remus, R.-S. 2015, MNRAS, 448, 1504
Tinker, J., Kravtsov, A. V., Klypin, A., et al. 2008, ApJ, 688, 709
Tinker, J. L., Robertson, B. E., Kravtsov, A. V., et al. 2010, ApJ, 724, 878
Tormen, G. 1998, MNRAS, 297, 648
Tormen, G., Diaferio, A., & Syer, D. 1998, MNRAS, 299, 728
Tormen, G., Moscardini, L., & Yoshida, N. 2004, MNRAS, 350, 1397
Tornatore, L., Borgani, S., Dolag, K., & Matteucci, F. 2007, MNRAS, 382, 1050
Umetsu, K. 2020, A&A Rev., 28, 7
Umetsu, K., Sereno, M., Lieu, M., et al. 2020, ApJ, 890, 148
Velliscig, M., van Daalen, M. P., Schaye, J., et al. 2014, MNRAS, 442, 2641
Wu, H.-Y., Costanzi, M., To, C.-H., et al. 2022, MNRAS, 515, 4471
Zhao, D. H., Jing, Y. P., Mo, H. J., & Bnörner, G. 2009, ApJ, 707, 354
Zohren, H., Schrabback, T., Bocquet, S., et al. 2022, A&A, 668, A18

[1] INAF-Osservatorio di Astrofisica e Scienza dello Spazio di Bologna, Via Piero Gobetti 93/3, 40129 Bologna, Italy
[2] INFN-Sezione di Bologna, Viale Berti Pichat 6/2, 40127 Bologna, Italy
[3] INAF-Osservatorio Astronomico di Trieste, Via G. B. Tiepolo 11, 34143 Trieste, Italy
[4] IFPU, Institute for Fundamental Physics of the Universe, via Beirut 2, 34151 Trieste, Italy
[5] Dipartimento di Fisica - Sezione di Astronomia, Universitá di Trieste, Via Tiepolo 11, 34131 Trieste, Italy
[6] INFN, Sezione di Trieste, Via Valerio 2, 34127 Trieste TS, Italy
[7] Institut für Theoretische Astrophysik, Zentrum für Astronomie, Heidelberg Universität, Albert-Ueberle-Str. 2, 69120, Heidelberg, Germany
[8] Dipartimento di Fisica e Astronomia "Augusto Righi" - Alma Mater Studiorum Università di Bologna, via Piero Gobetti 93/2, 40129 Bologna, Italy
[9] Departamento de Física Teórica, Facultad de Ciencias, Universidad Autónoma de Madrid, 28049 Cantoblanco, Madrid, Spain
[10] Centro de Investigación Avanzada en Física Fundamental (CIAFF), Facultad de Ciencias, Universidad Autónoma de Madrid, 28049 Madrid, Spain
[11] Institute for Astronomy, University of Edinburgh, Royal Observatory, Blackford Hill, Edinburgh EH9 3HJ, UK
[12] International Centre for Radio Astronomy Research, University of Western Australia, 35 Stirling Highway, Crawley, Western Australia 6009, Australia
[13] Laboratoire Univers et Théorie, Observatoire de Paris, Université PSL, Université Paris Cité, CNRS, 92190 Meudon, France
[14] AIM, CEA, CNRS, Université Paris-Saclay, Université de Paris, 91191 Gif-sur-Yvette, France
[15] Institut für Astro- und Teilchenphysik, Universität Innsbruck, Technikerstr. 25/8, 6020 Innsbruck, Austria
[16] Argelander-Institut für Astronomie, Universität Bonn, Auf dem Hügel 71, 53121 Bonn, Germany
[17] Université Paris-Saclay, Université Paris Cité, CEA, CNRS, AIM, 91191, Gif-sur-Yvette, France
[18] Université Paris-Saclay, CNRS, Institut d'astrophysique spatiale, 91405, Orsay, France
[19] Institut für Theoretische Physik, University of Heidelberg, Philosophenweg 16, 69120 Heidelberg, Germany
[20] Max Planck Institute for Extraterrestrial Physics, Giessenbachstr. 1, 85748 Garching, Germany
[21] INAF-Osservatorio Astrofisico di Torino, Via Osservatorio 20, 10025 Pino Torinese (TO), Italy
[22] Dipartimento di Fisica, Università di Genova, Via Dodecaneso 33, 16146, Genova, Italy
[23] INFN-Sezione di Roma Tre, Via della Vasca Navale 84, 00146, Roma, Italy
[24] Department of Physics "E. Pancini", University Federico II, Via Cinthia 6, 80126, Napoli, Italy
[25] Instituto de Astrofísica e Ciências do Espaço, Universidade do Porto, CAUP, Rua das Estrelas, PT4150-762 Porto, Portugal
[26] Dipartimento di Fisica, Universitá degli Studi di Torino, Via P. Giuria 1, 10125 Torino, Italy
[27] INFN-Sezione di Torino, Via P. Giuria 1, 10125 Torino, Italy
[28] INAF-IASF Milano, Via Alfonso Corti 12, 20133 Milano, Italy
[29] Institut de Física d'Altes Energies (IFAE), The Barcelona Institute of Science and Technology, Campus UAB, 08193 Bellaterra (Barcelona), Spain
[30] Port d'Informació Científica, Campus UAB, C. Albareda s/n, 08193 Bellaterra (Barcelona), Spain
[31] Institut d'Estudis Espacials de Catalunya (IEEC), Carrer Gran Capitá 2-4, 08034 Barcelona, Spain
[32] Institute of Space Sciences (ICE, CSIC), Campus UAB, Carrer de Can Magrans, s/n, 08193 Barcelona, Spain
[33] INAF-Osservatorio Astronomico di Roma, Via Frascati 33, 00078 Monteporzio Catone, Italy
[34] INAF-Osservatorio Astronomico di Capodimonte, Via Moiariello 16, 80131 Napoli, Italy
[35] INFN section of Naples, Via Cinthia 6, 80126, Napoli, Italy
[36] Centre National d'Etudes Spatiales, Toulouse, France
[37] Institut national de physique nucléaire et de physique des particules, 3 rue Michel-Ange, 75794 Paris Cédex 16, France
[38] Jodrell Bank Centre for Astrophysics, Department of Physics and Astronomy, University of Manchester, Oxford Road, Manchester M13 9PL, UK
[39] ESAC/ESA, Camino Bajo del Castillo, s/n., Urb. Villafranca del Castillo, 28692 Villanueva de la Cañada, Madrid, Spain
[40] European Space Agency/ESRIN, Largo Galileo Galilei 1, 00044 Frascati, Roma, Italy
[41] Univ Lyon, Univ Claude Bernard Lyon 1, CNRS/IN2P3, IP2I Lyon, UMR 5822, 69622, Villeurbanne, France
[42] Institute of Physics, Laboratory of Astrophysics, Ecole Polytechnique Fédérale de Lausanne (EPFL), Observatoire de Sauverny, 1290 Versoix, Switzerland
[43] Mullard Space Science Laboratory, University College London, Holmbury St Mary, Dorking, Surrey RH5 6NT, UK
[44] Departamento de Física, Faculdade de Ciências, Universidade de Lisboa, Edifício C8, Campo Grande, PT1749-016 Lisboa, Portugal
[45] Instituto de Astrofísica e Ciências do Espaço, Faculdade de Ciências, Universidade de Lisboa, Campo Grande, 1749-016 Lisboa, Portugal
[46] Department of Astronomy, University of Geneva, ch. d'Ecogia 16, 1290 Versoix, Switzerland
[47] INFN-Padova, Via Marzolo 8, 35131 Padova, Italy
[48] Université Paris-Saclay, Université Paris Cité, CEA, CNRS, Astrophysique, Instrumentation et Modélisation Paris-Saclay, 91191 Gif-sur-Yvette, France
[49] INAF-Osservatorio Astronomico di Padova, Via dell'Osservatorio 5, 35122 Padova, Italy
[50] Universitäts-Sternwarte München, Fakultät für Physik, Ludwig-Maximilians-Universität München, Scheinerstrasse 1, 81679 München, Germany
[51] Institute of Theoretical Astrophysics, University of Oslo, P.O. Box 1029 Blindern, 0315 Oslo, Norway
[52] Jet Propulsion Laboratory, California Institute of Technology, 4800 Oak Grove Drive, Pasadena, CA, 91109, USA
[53] Technical University of Denmark, Elektrovej 327, 2800 Kgs. Lyngby, Denmark
[54] Cosmic Dawn Center (DAWN), Denmark
[55] Max-Planck-Institut für Astronomie, Königstuhl 17, 69117 Heidelberg, Germany
[56] Aix-Marseille Université, CNRS/IN2P3, CPPM, Marseille, France
[57] Université de Genève, Département de Physique Théorique and Centre for Astroparticle Physics, 24 quai Ernest-Ansermet, CH-1211 Genève 4, Switzerland
[58] Department of Physics, P.O. Box 64, 00014 University of Helsinki, Finland
[59] Helsinki Institute of Physics, Gustaf Hällströmin katu 2, University of Helsinki, Helsinki, Finland
[60] NOVA optical infrared instrumentation group at ASTRON, Oude Hoogeveensedijk 4, 7991PD, Dwingeloo, The Netherlands

[61] Department of Physics, Institute for Computational Cosmology, Durham University, South Road, DH1 3LE, UK
[62] Université Côte d'Azur, Observatoire de la Côte d'Azur, CNRS, Laboratoire Lagrange, Bd de l'Observatoire, CS 34229, 06304 Nice cedex 4, France
[63] Université Paris Cité, CNRS, Astroparticule et Cosmologie, 75013 Paris, France
[64] European Space Agency/ESTEC, Keplerlaan 1, 2201 AZ Noordwijk, The Netherlands
[65] Leiden Observatory, Leiden University, Niels Bohrweg 2, 2333 CA Leiden, The Netherlands
[66] Kapteyn Astronomical Institute, University of Groningen, PO Box 800, 9700 AV Groningen, The Netherlands
[67] Department of Physics and Astronomy, University of Aarhus, Ny Munkegade 120, DK-8000 Aarhus C, Denmark
[68] Space Science Data Center, Italian Space Agency, via del Politecnico snc, 00133 Roma, Italy
[69] Institute of Space Science, Bucharest, 077125, Romania
[70] Dipartimento di Fisica e Astronomia "G.Galilei", Universitá di Padova, Via Marzolo 8, 35131 Padova, Italy
[71] Dipartimento di Fisica e Astronomia, Universitá di Bologna, Via Gobetti 93/2, 40129 Bologna, Italy
[72] Departamento de Física, FCFM, Universidad de Chile, Blanco Encalada 2008, Santiago, Chile
[73] Institut de Ciencies de l'Espai (IEEC-CSIC), Campus UAB, Carrer de Can Magrans, s/n Cerdanyola del Vallés, 08193 Barcelona, Spain
[74] Centro de Investigaciones Energéticas, Medioambientales y Tecnológicas (CIEMAT), Avenida Complutense 40, 28040 Madrid, Spain
[75] Instituto de Astrofísica e Ciências do Espaço, Faculdade de Ciências, Universidade de Lisboa, Tapada da Ajuda, 1349-018 Lisboa, Portugal
[76] Universidad Politécnica de Cartagena, Departamento de Electrónica y Tecnología de Computadoras, 30202 Cartagena, Spain
[77] Institut de Recherche en Astrophysique et Planétologie (IRAP), Université de Toulouse, CNRS, UPS, CNES, 14 Av. Edouard Belin, 31400 Toulouse, France
[78] Infrared Processing and Analysis Center, California Institute of Technology, Pasadena, CA 91125, USA
[79] INAF-Osservatorio Astronomico di Brera, Via Brera 28, 20122 Milano, Italy
[80] Instituto de Astrofísica de Canarias, Calle Vía Láctea s/n, 38204, San Cristóbal de La Laguna, Tenerife, Spain
[81] Center for Computational Astrophysics, Flatiron Institute, 162 5th Avenue, 10010, New York, NY, USA
[82] School of Physics and Astronomy, Cardiff University, The Parade, Cardiff, CF24 3AA, UK
[83] INAF-Istituto di Astrofisica e Planetologia Spaziali, via del Fosso del Cavaliere, 100, 00100 Roma, Italy
[84] Ernst-Reuter-Str. 4e, 31224 Peine, Germany
[85] Department of Physics and Helsinki Institute of Physics, Gustaf Hällströmin katu 2, 00014 University of Helsinki, Finland
[86] Dipartimento di Fisica e Astronomia "Augusto Righi" - Alma Mater Studiorum Universitá di Bologna, Viale Berti Pichat 6/2, 40127 Bologna, Italy
[87] Institut d'Astrophysique de Paris, 98bis Boulevard Arago, 75014, Paris, France
[88] Junia, EPA department, 59000 Lille, France
[89] INFN-Bologna, Via Irnerio 46, 40126 Bologna, Italy
[90] Instituto de Física Teórica UAM-CSIC, Campus de Cantoblanco, 28049 Madrid, Spain
[91] CERCA/ISO, Department of Physics, Case Western Reserve University, 10900 Euclid Avenue, Cleveland, OH 44106, USA
[92] Laboratoire de Physique de l'École Normale Supérieure, ENS, Université PSL, CNRS, Sorbonne Université, 75005 Paris, France
[93] Observatoire de Paris, Université PSL, Sorbonne Université, LERMA, 750 Paris, France
[94] Astrophysics Group, Blackett Laboratory, Imperial College London, London SW7 2AZ, UK
[95] SISSA, International School for Advanced Studies, Via Bonomea 265, 34136 Trieste TS, Italy
[96] Dipartimento di Fisica e Scienze della Terra, Universitá degli Studi di Ferrara, Via Giuseppe Saragat 1, 44122 Ferrara, Italy
[97] Istituto Nazionale di Fisica Nucleare, Sezione di Ferrara, Via Giuseppe Saragat 1, 44122 Ferrara, Italy
[98] Institut de Physique Théorique, CEA, CNRS, Université Paris-Saclay 91191 Gif-sur-Yvette Cedex, France
[99] Institut d'Astrophysique de Paris, UMR 7095, CNRS, and Sorbonne Université, 98 bis boulevard Arago, 75014 Paris, France
[100] NASA Ames Research Center, Moffett Field, CA 94035, USA
[101] INAF, Istituto di Radioastronomia, Via Piero Gobetti 101, 40129 Bologna, Italy
[102] Institute for Theoretical Particle Physics and Cosmology (TTK), RWTH Aachen University, 52056 Aachen, Germany
[103] Institute for Astronomy, University of Hawaii, 2680 Woodlawn Drive, Honolulu, HI 96822, USA
[104] Department of Physics & Astronomy, University of California Irvine, Irvine CA 92697, USA
[105] University of Lyon, UCB Lyon 1, CNRS/IN2P3, IUF, IP2I Lyon, France
[106] INFN-Sezione di Genova, Via Dodecaneso 33, 16146, Genova, Italy
[107] Aix-Marseille Université, CNRS, CNES, LAM, Marseille, France
[108] Department of Astronomy & Physics and Institute for Computational Astrophysics, Saint Mary's University, 923 Robie Street, Halifax, Nova Scotia, B3H 3C3, Canada
[109] University Observatory, Faculty of Physics, Ludwig-Maximilians-Universität, Scheinerstr. 1, 81679 Munich, Germany
[110] Ruhr University Bochum, Faculty of Physics and Astronomy, Astronomical Institute (AIRUB), German Centre for Cosmological Lensing (GCCL), 44780 Bochum, Germany
[111] Department of Physics, Lancaster University, Lancaster, LA1 4YB, UK
[112] Univ. Grenoble Alpes, CNRS, Grenoble INP, LPSC-IN2P3, 53, Avenue des Martyrs, 38000, Grenoble, France
[113] Department of Physics and Astronomy, University College London, Gower Street, London WC1E 6BT, UK
[114] Department of Physics and Astronomy, Vesilinnantie 5, 20014 University of Turku, Finland
[115] Centre de Calcul de l'IN2P3, 21 avenue Pierre de Coubertin 69627 Villeurbanne Cedex, France
[116] Dipartimento di Fisica, Sapienza Università di Roma, Piazzale Aldo Moro 2, 00185 Roma, Italy
[117] University of Applied Sciences and Arts of Northwestern Switzerland, School of Engineering, 5210 Windisch, Switzerland
[118] INFN-Sezione di Roma, Piazzale Aldo Moro, 2 - c/o Dipartimento di Fisica, Edificio G. Marconi, 00185 Roma, Italy
[119] Centro de Astrofísica da Universidade do Porto, Rua das Estrelas, 4150-762 Porto, Portugal
[120] Institute of Cosmology and Gravitation, University of Portsmouth, Portsmouth PO1 3FX, UK
[121] Department of Mathematics and Physics E. De Giorgi, University of Salento, Via per Arnesano, CP-I93, 73100, Lecce, Italy
[122] INFN, Sezione di Lecce, Via per Arnesano, CP-193, 73100, Lecce, Italy
[123] INAF-Sezione di Lecce, c/o Dipartimento Matematica e Fisica, Via per Arnesano, 73100, Lecce, Italy
[124] CEA Saclay, DFR/IRFU, Service d'Astrophysique, Bat. 709, 91191 Gif-sur-Yvette, France
[125] Institute for Computational Science, University of Zurich, Winterthurerstrasse 190, 8057 Zurich, Switzerland
[126] Université St Joseph; Faculty of Sciences, Beirut, Lebanon
[127] Dipartimento di Fisica "Aldo Pontremoli", Universitá degli Studi di Milano, Via Celoria 16, 20133 Milano, Italy